Title

Structural and biochemical analysis of ligand binding in yeast Niemann-Pick type C1-related protein

Running title

Substrate scope of yeast NCR1 and NPC2

Authors

Lynette Nel[1]*, Katja Thaysen[2]*, Denisa Jamecna[3]*, Esben Olesen[1], Maria Szomek[2], Julia Langer[3], Kelly May Frain[1], Doris Höglinger[3], Daniel Wüstner[2#], Bjørn P. Pedersen[1#]

[1]Department of Molecular Biology and Genetics, Aarhus University, Aarhus C 8000, Denmark.
[2]Department of Biochemistry and Molecular Biology, University of Southern Denmark, 5230 Odense M, Denmark.
[3]Heidelberg University, Biochemistry Center, Ruprecht-Karls-Universität Heidelberg, 69120 Heidelberg, Germany.
*Contributed equally to this work
[#]Corresponding authors: wuestner@bmb.sdu.dk and bpp@mbg.au.dk

Keywords

lipids; Niemann-Pick type C1-related protein; NPC; sphingosine; sterol homeostasis; vacuole

Summary blurb

Results of X-ray crystallography and binding assays with different lipids expand our knowledge of the substrate scope of the Niemann-Pick type C1-related proteins NCR1 and NPC2 in yeast.

Abstract

In eukaryotes, integration of sterols into the vacuolar/lysosomal membrane is critically dependent on the Niemann-Pick type C (NPC) system. The system consists of an integral membrane protein, called NCR1 in yeast, and NPC2, a luminal soluble protein that transfers sterols to the N-terminal domain (NTD) of NCR1 before membrane integration. Both proteins have been implicated in sterol homeostasis of yeast and humans. Here, we investigate sterol and lipid binding of the NCR1/NPC2 transport system and determine crystal structures of the sterol-binding NTD. The NTD binds both ergosterol and cholesterol, with nearly identical conformations of the binding pocket. Apart from sterols, the NTD can also bind fluorescent analogs of phosphatidylinositol, phosphatidylcholine and phosphatidylserine as well as sphingosine and ceramide. We confirm the multi-lipid scope of the NCR1/NPC2 system using photo-crosslinkable and clickable lipid analogs, namely pac-cholesterol, pac-sphingosine and pac-ceramide. Finally, we reconstitute the transfer of pac-sphingosine from NPC2 to the NTD *in vitro*. Collectively, our results support that the yeast NPC system can work as versatile machinery for vacuolar homeostasis of structurally diverse lipids, besides ergosterol.

MAIN TEXT:

INTRODUCTION

Sterols are indispensable components of membranes in all eukaryotic cells and precursors to many metabolites, which are required for various cellular processes (1,2,3). Endogenous sterols are synthesized at the endoplasmic reticulum and exogenous sterols can enter the cell through, for example, endocytosis (4). The redistribution of sterols to all membranes of the cell occurs, for instance, at acidic organelles called lysosomes in animals and vacuoles in fungi and plants (5,6,7,8,9,10,11). The luminal membrane of lysosomes and vacuoles is lined with a glycocalyx, a polysaccharide matrix that prevents autodigestion by resident hydrolytic enzymes (12,13,14,15,16).

In humans, Niemann-Pick type C (NPC) disease is a lysosomal storage disorder characterized by intra-lysosomal accumulation (storage) of cholesterol and sphingolipids, typically manifesting as progressive neurological dysfunction in children (17,18). The disease arises from mutations in genes encoding either Niemann-Pick type C1 protein (hNPC1, an integral membrane protein) that integrates sterols into the lysosomal membrane, or Niemann-Pick type C2 protein (hNPC2, a soluble protein inside the lysosomal lumen) that delivers sterols to hNPC1 (19,20,21,22). Homologs of both proteins are found in all eukaryotes. The vacuole of *Saccharomyces cerevisiae* contains Nieman-Pick type C1-related protein 1 (NCR1) as well as NPC2. Notably, NCR1 and NPC2 can rescue the disease phenotype in NPC-deficient mammalian cells, making it a suitable model system to better understand NPC disease as well as eukaryotic sterol and lipid homeostasis in general (23,24).

NPC2 proteins consist of seven anti-parallel β-sheets that form a hydrophobic sterol-binding pocket, with NPC2 having a ~5 fold larger binding pocket compared to that of human and bovine NPC2 (25,26,27,28). NCR1 and hNPC1 share the same structural fold; an N-terminal domain (NTD), a middle-luminal domain (MLD) and a C-terminal domain (CTD) found on the luminal side of the vacuolar/lysosomal membrane. Thirteen transmembrane helices (M1-M13) span the membrane, of which M1 anchors the NTD to the vacuolar/lysosomal membrane, while the remaining 12 transmembrane helices are divided into a sterol-sensing domain (SSD, M2-M7) and a pseudo-SSD domain (pSSD, M8-M13) (14,22,27,29,30). This fold is characteristic of the resistance-nodulation-division (RND) superfamily, but with the NTD and M1 helix being unique features found only in NPC proteins (31,32). The current transport model for the NPC system postulates that NPC2 binds sterols in the lumen, loads them into the NTD, which transfers the sterol to a tunnel that is formed by the MLD and CTD of hNPC1 and NCR1, respectively (1,27,33,34). This tunnel, essential to bypassing the glycocalyx, changes shape depending on the protonation state of key residues in the SSD and pSSD, to transport the sterol to the luminal membrane for membrane integration (Figure 1A) (14,22).

It has been shown that the NTD of hNPC1 binds cholesterol and 25-hydroxycholesterol tightly (35). The binding pocket of hNPC2 can accommodate a variety of sterols including cholesterol, epi-cholesterol and cholesteryl sulfate but its affinity for oxysterols is much lower (36,37,38). Synthesis and transport of cholesterol derivatives, such as 25- and 27-hydroxycholesterol, are disturbed when cells lack hNPC2, but this protein is not strictly needed to transport fluorescent analogs of 25- and 27-hydroxycholesterol out of the lysosomes in human fibroblasts from NPC disease patients (36,38,39). In addition to sterols, hNPC2 interacts with various phospholipids, of which the highest relative binding was observed for lysobisphosphatidic acid, a lysosomal-specific phospholipid (40). It was previously shown that the large binding pocket of yeast NPC2 enables it to bind a variety of substrates *in vitro*, such as edelfosine (a lipid analog with antifungal properties), (41,42), U18666A (a cationic sterol that inhibits Ebola infection through NPC1) (43), sterols, phospholipids and sphingolipids (27,28). The broad substrate-binding capacity of yeast NPC2, when compared with the human counterpart, and its capability to transfer sterols to the NTD of NCR1 led to the speculation that the NTD might bind a diverse range of lipids, and not only sterols (27,28).

In this study, we examine the substrate specificity of the NTD of NCR1 and NPC2. We describe structures of the NTD bound to either ergosterol or cholesterol and analyze the architecture of the substrate binding pocket. *In vitro* binding of ligand candidates to delipidated NTD and NPC2 are evaluated using nitrobenzoxadiazole (NBD)-tagged lipids as well as photo-activatable and clickable (pac-) lipids (28,44,45,46). The results indicate that the NTD and NPC2 bind pac-modified cholesterol, and NBD- and pac-phospholipids and sphingolipids. Lastly, we demonstrate that NPC2 can transfer pac-sphingosine to the NTD. Overall, these results expand our knowledge regarding the capacity of NPC2 and NCR1 to bind a range of hydrophobic ligands.

RESULTS

Ergosterol- and cholesterol-bound structures of the NTD

To study the substrate scope of NCR1, the NTD (residue 1-249 of NCR1) was purified and crystallized with either ergosterol or cholesterol (Figure S1A, Table S1): ergosterol-bound at 2.4 Å (R_{free} 26%) and cholesterol-bound at 2.6 Å (R_{free} 26%) (Figure 1B to 1F). Besides the sterol, the two structures show minimal differences between them (root mean square deviation of C-alpha atoms, $RMSD_{C\alpha}$ of 0.39 Å). In the asymmetric unit, there are four monomers of the NTD, with no structural differences between monomers ($RMSD_{C\alpha}$ of 0.13 to 0.26 Å).

The architecture of the NTD consists of seven α-helices and a three-strand mixed β-sheet (Figure 1B). All 16 cysteine residues form disulfide bridges and are partitioned to the side facing the other luminal domains of NCR1 (Figure S1B). Three residues (N123, N145 and N178) are N-glycosylated and deglycosylation of purified NTD yielded a sample that was reduced by ~8 kDa, (equivalent to about 44 mannose units) (Figure S1C). Both structures were derived from glycosylated samples and show long glycosylation chains that extend from the "back" of the NTD, the opposing side to the substrate binding pocket (Figure S1B and S1D). The glycan chains are well-structured and three to seven can be modeled per glycosylation site, in some to the point where the glycan chain starts to branch (Figure S1E).

Clear density of an ion in a well-defined cation coordination site on the "back" of the NTD was identified (Figure 2A). Since $ZnSO_4$ was used in the crystallization solution, a zinc ion was modeled. The site is formed by E67 (on the loop connecting helix 1 and 2), N107, H111 (both on helix 3) and D218 (on the loop that becomes the linker toward M1).

Ergosterol and cholesterol are highly similar in their chemical structure (Figure 1C and Figure 1E), but the quality of the electron density maps allows for clear discernment between the two in the NTD binding pocket. In particular, the double bond between C22 and C23 of ergosterol results in a more rigid iso-octyl chain, evident as density that is continuous with the ring system (Figure 1C). Cholesterol lacks this double bond in the iso-octyl chain, making it more flexible and this is observed as density that is discontinuous with the ring system (Figure 1E). The substrate binding pockets of the two structures are virtually identical, with both substrates positioned parallel to helix 2 (Figure 2B). The interior of the substrate binding pocket is lined with hydrophobic residues, except for Q80, T113 and S196 – with Q80 coordinating the hydroxyl group of the sterol (Figure 1 D and Figure 1F). F109 and F112 are positioned underneath the ligand, allowing for pi-stacking with the sterol ring system. Minor differences between the two structures are observed in three mobile loops: the "mobile loop 1" to helix 1, "mobile loop 2" connects helix 5 to helix 6 and "mobile loop 3" connects helix 7 to strand 3 (Figure 2C). Upon comparison, the position of "mobile loop 2" is displaced the most when aligning the ergosterol- and cholesterol-bound structures.

The binding pocket of the NTD is closed off by a "ridge", formed by the sidechain of K90 and the backbone carboxyl group of G194 (6.1 Å apart), dividing the binding pocket into a "sterol opening" and "water opening" (Figure 2D). Additionally, N37 and N87 partially cover the "water-opening", with

their sidechains ~6 Å apart. In this way, the binding mode of the sterol is with the hydrophilic headgroup the deepest in the pocket, while the hydrophobic tail extends toward the sterol opening.

The NTD and NPC2 bind a range of NBD-tagged lipids

To investigate substrate candidates for the NTD of NCR1 and NPC2, biochemical assays were conducted with purified protein and fluorescent lipid analogues. The purified, delipidated NTD was titrated into nitrobenzoxadiazole (NBD)-tagged phospho- and sphingolipids, in which the fluorophore is attached to the hydrophobic tail of the lipid molecules. An increase in signal is based on an enhanced molecular brightness of the NBD-moiety upon binding in a more hydrophobic environment (28). This increase in fluorescence correlates with the concentration of the NTD (Figure 3A), which can be used to infer the affinity of the NTD to a given NBD-lipid (Figure 3B to 3G). Binding curves of the NTD with five NBD-lipids were obtained: phosphatidylcholine (NBD-PC), phosphatidylinositol (NBD-PI), phosphatidylserine (NBD-PS), ceramide (NBD-Cer) and sphingosine (NBD-Sph) (Figure 3B to 3G). The measured increase in fluorescence of each NBD-lipid upon titrating the protein was used to determine an apparent dissociation constant (K_D) according to a one-site binding model (Equation 1).

Most measurements were carried out at pH 5.5 to mimic the physiological pH of the vacuole, but the affinity of the NTD to NBD-lipids at neutral pH (7.5) was also assessed. The NTD has the strongest binding affinity for NBD-PI (K_D = 213 nM) and NBD-Sph (K_D = 254 nM), followed by NBD-PC (K_D = 569 nM), NBD-PS (K_D = 928 nM) and NBD-Cer (K_D = 1264 nM) at pH 5.5 (Table 1). For NBD-PI and NBD-Sph, the concentration used in the binding assays of 1 µM is below their respective critical micelle concentration (CMC), which was measured to be 2.3 µM for NBD-PI (28) and ~12 µM for NBD-Sph with the same assay (Figure S4A). Thus, for these two lipids, the increase in NBD-fluorescence likely comes from a higher quantum yield of the fluorophore inside the binding pocket but not from dequenching, as observed for micelles of NBD-lipids (28). Measurements with NBD-Sph revealed a two-fold stronger binding affinity at neutral compared to acidic pH (K_D = 115 nM compared to K_D = 254 nM, Figure 3F and 3G). This change in binding affinity of NBD-Sph to the NTD of NCR1 could be caused by an altered hydrogen binding capacity of the sphingosine backbone when the pH changes, as has been shown to take place for natural sphingosine (47). The latter has a pKa of 6.61 in the aggregated form, so an alteration in the protonation state of NBD-Sph at pH 7.5 compared to pH 5.5 could influence the affinity of NBD-Sph to the NTD.

The ability of NPC2 to bind phospholipids has been shown before (28). In the current study, the binding of NBD-Cer and NBD-Sph to purified NPC2 was assessed to compare with that of the NTD. At pH 5.5, the binding affinity of NPC2 for NBD-Cer (K_D = 91 nM, Figure S3A) is stronger compared to that of the NTD (K_D = 1264 nM, Figure 3E). Both NPC2 and the NTD bind NBD-Sph, but the NTD has higher affinity (K_D = 254 nM at pH 5.5, and K_D = 115 nM at pH 7.5, Figure 3G and 3F) than NPC2 (K_D = 580 nM at pH 5.5, and K_D = 530 nM at pH 7.5, Figure S3B and 3C).

Edelfosine is a synthetic lysophospholipid with cytotoxic antifungal effects. Yeast strains with NCR1 knocked out are resistant to this compound, suggesting that edelfosine is a ligand of NCR1 (41). To investigate this, two competitive binding assays with edelfosine and NBD-Sph were designed (Figure 4). For the first assay, the NTD was saturated by NBD-Sph and the addition of edelfosine led to the exchange of NTD-bound substrate, causing a drop in NBD-Sph fluorescence by about 50% (Figure 4A). The CMC of edelfosine is measured to be 715 nM (Figure S4B), thus, after exceeding this concentration of edelfosine, excess NBD-Sph can participate in micelle formation, which is most likely what is observed as an intensity increase after addition of 1 µM edelfosine to 1 µM NBD-Sph (Figure S4C). Interestingly, the raw intensities of NBD-Sph at maximal concentration of edelfosine are comparable in the presence and absence of the NTD (not shown). This suggests that the majority of NBD-Sph is efficiently outcompeted and replaced by edelfosine in the binding pocket of the NTD. To further evaluate the capability of NBD-Sph to participate in micelle formation, each emission spectrum

was normalized with varying concentrations of edelfosine (Figure 4B). Emission peaks at ~550 nm for NBD-Sph were observed at low concentrations of edelfosine, however, at concentrations exceeding 1 μM of edelfosine, the emission peaks shift to ~540 nm. The shift in wavelength of the emission peaks indicates a change in the environment of the fluorophore (48,49,50), likely indicating the transition of NBD-Sph from being free in solution to being incorporated into mixed micelles with edelfosine. Initially, emission peaks at ~530 nm are observed, assigned to be NTD and NBD-Sph complexes (Figure 4C). As the edelfosine concentration exceeds 2-3 μM, the emission peaks shift towards 540 nm, suggesting that edelfosine effectively outcompetes NBD-Sph, causing NBD-Sph to form micelles. Similarly, binding of substrates at higher concentrations than their CMC, this binding assay is rather complex due to edelfosine exceeding its CMC. Furthermore, Equation 1 does not account for NBD-Sph being able to participate in micelle formation. Due to these restrictions, the inhibitory constant for edelfosine is referred to as apparent, rather than a real inhibitor constant (K_I). Equation 2 was used to determine the K_I as 49 nM based on a half-maximal inhibitory concentration (IC50) of 0.48 μM derived from Figure 4A. This suggests that the NTD binds edelfosine more strongly than NBD-Sph, explaining why edelfosine can outcompete NBD-Sph.

Based on the above observations, fixed amounts of edelfosine were added to NBD-Sph prior to titrating with the NTD in the second assay (Figure 4D). The measurements show that more NTD is needed to saturate the binding of NBD-Sph as the edelfosine concentration increases, suggesting that NBD-Sph and edelfosine compete for the binding pocket of the NTD. This observation is confirmed by the increase in apparent K_D-values of NBD-Sph from 115 nM to 209 nM as the edelfosine concentration was raised. Together, results from both assays demonstrate that edelfosine is likely a ligand of NCR1 and that it binds tighter to the NTD than NBD-Sph.

The NTD and NPC2 crosslink to photo-activatable and clickable lipid analogs

In a parallel approach, the substrate scope of the NTD and NPC2 was probed with photo-activatable and clickable (pac) lipids. Pac-lipids contain small chemical modifications for click chemistry reactions, with fluorophores such as AF647 (a structural analog of Alexa Fluor® 647), and for UV-activated photo-crosslinking, respectively (45). In contrast to NBD-tagged lipids delivered in solution, pac-lipids such as pac-cholesterol (pacChol), pac-phosphatidylcholine (pacPC), pac-sphingosine (pacSph) and pac-ceramide (pacCer) were reconstituted in liposomal membranes (Figure 5A). As expected, the delipidated NTD crosslinks with pacChol (average +UV/-UV ratio = 2.11). Crosslinking of the NTD with pacSph (+UV / -UV = 1.73) and, to a lesser extent, with pacCer and pacPC (+UV/-UV = 1.40 and 1.12), respectively, were also detected Figure 5B and 5C).

To compare with the interaction profile of the NTD, crosslinking assays were also performed with purified, delipidated NPC2 (Figure S5A and S5B). In general, NPC2 displays higher +UV/-UV ratios, suggesting a more efficient lipid binding, likely due to its large hydrophobic cavity (27). NPC2 crosslinks well with all tested pac-lipids but, as for the NTD, most strongly with pacChol (+UV/-UV ratio = 1.91). Robust and consistent crosslinking with pacSph (+UV/-UV ratio = 1.64), pacCer (+UV/-UV = 1.67) and pacPC (+UV/-UV = 1.63) were observed. The crosslinking efficiency for cholesterol and sphingosine analogs was higher for the NTD, whereas crosslinking with ceramide and PC analogs seemed stronger with NPC2.

The consistent interaction of sphingosine with both the NTD and NPC2 observed in this study inspired us to examine whether the transfer of pacSph between the two proteins could be reconstituted *in vitro*. To this end, a protein-to-protein sphingosine transfer assay using solubilized, free pacSph, was designed (Figure 6A). To correct for non-specific fluorophore background, His-tagged green fluorescent protein (His-sfGFP) was used since it does not crosslink with pac-lipids (our own unpublished observation). As a control for specificity of transfer, the lipid binding domain of a mammalian STARD3 (His-STARD3-StART) was used since this protein was previously shown to interact with sphingosine

in related work (51, preprint) but it is not located inside lysosomes and, therefore, is not expected to interact with the NTD. His-tagged NPC2, His-sfGFP or His-STARD3-StART were immobilized on Ni-NTA beads, pre-loaded with pacSph, and incubated with the NTD. After removal of the beads, the NTD was subjected to UV-crosslinking, clicked with a fluorophore and the resulting lipid-protein complexes were visualized by SDS-PAGE. Our results reveal increased crosslinking between pacSph and the NTD when pacSph was delivered by NPC2, but not when it was delivered by GFP or STARD3 (Figure 6B and 6C). Similar assays with pacCer did not yield positive results (Figure S6). Together, these results support the specific transfer of pacSph from NPC2 to the NTD and indicate the ability of the yeast NPC system to export vacuolar sphingosine.

Lastly, the impact of "competitive" lipids on the crosslinking profile of the scNPC2 was investigated since the spectroscopy assays show that edelfosine competes with NBD-sphingosine binding to the NTD (Figure 4). Previous reports also show that edelfosine decreases the binding of radioactive cholesterol by the NTD (27). To explore this further, pac-lipid-containing liposomes were supplemented with 5-fold excess of edelfosine, however, no noticeable inhibition of crosslinking was observed (Figure S7A and S7B). In a similar way, the effects of ergosterol on protein-lipid interaction were evaluated. Ergosterol does not visibly influence the crosslinking with pacChol and pacPC, whereas a trend towards increased crosslinking with pacSph and pacCer is observed (Figure S7C and S7D).

DISCUSSION

X-ray crystallography was used to solve structures of the NTD, from *S. cerevisiae*, bound to ergosterol and cholesterol (Table S1). The binding pocket of the two structures are virtually identical, with only K90 adopting a slightly different rotamer (Figure 2B) but still capable of interacting with the backbone of G194 to form a "ridge" across the binding pocket, creating the "sterol-opening" and "water-opening" (Figure 2D). The binding pocket itself is lined mainly with hydrophobic residues, in particular, F109 and F112 pi-stack with the ring system of a sterol for strong binding (Figure 1D, Figure 1F and Figure 2B). One of the polar residues, Q80, interacts with the hydroxyl group of the sterol at the deepest point of the binding pocket. Three regions that do change in position are loops on the face of the substrate binding pocket, of which "mobile loop 3" contains the "ridge" that spans the binding pocket (Figure 2C and Figure 2D). The most displaced loop is "mobile loop 2" at the top of the "sterol-opening". Together, "mobile loop 2" and "mobile loop 3" likely gate substrate entry and exit. The regions proposed to govern substrate accessibility of the NTD from hNPC1 differ from what is proposed here for the NTD (Figure S2A), particularly helix 3, helix 7 and helix 8 of the NTD from hNPC1, all at the top of "sterol-opening", which excludes the ridge-forming mobile loop of the NTD (33).

Most of the residues conserved between the NTD and the NTD from hNPC1 are in the binding pocket (Figure S2A). Structurally, however, the substrate binding pocket of the NTD from yeast is less occluded, with 10.2 Å between K90 and I172, compared to 8.1 Å between the equivalent residues in the NTD of hNPC1 (Figure 2B and Figure S2B). Even though the binding pocket of the NTD is less occluded, cholesterol seems to bind 1.0 Å deeper compared to the NTD from hNPC1 (Figure S2B). The observation of cholesteryl-hemisuccinate (CHS) in the tunnel of full-length NCR1 supports the capability of the NTD to also bind sterols that are modified at the hydroxyl group (14), whereas the NTD of hNPC1 cannot (33). Similarly, the binding pocket of yeast NPC2 is larger than that of human NPC2 (27), which coincides with the NTD being able to accept a variety of substrates from NPC2 (28). The spacious binding mode of the NTD might allow other substrates, like single chain lipids, to fit in the binding pocket, where the polar headgroup would be enveloped by the protein and the hydrophobic tail would be positioned towards the "sterol-opening".

When comparing the NTD with the NTD from hNPC1, some unique features were observed. Only two of the five N-glycosylated residues of the NTD from hNPC1 (N122 and N185) (33) are conserved in the NTD (N123 and N178) (Figure S2A), however, all glycosylation sites are on the

opposite face of the substrate binding pocket (Figure S1B and Figure S1D), thus not interfering with sterol loading by NPC2. An ion coordination site, also opposite the substrate binding pocket, has not been described before (Figure 2A). It is not seen in the structures of full-length NCR1 and it does not seem to exist in the NTD from hNPC1. While it is possible that this ion coordination was an artifact of the crystallization process, it is known that the vacuole stores transition metal and calcium ions (52,53,54), which the NTD seems capable of binding. Lastly, an extension of the substrate binding pocket downward, terminating next to the ion coordination site, is seen in the NTD (Figure S2C). The ~20 Å long pocket is solvent accessible until a bottleneck (<1.4 Å) is formed by L108, F121 and F216.

When comparing the position of ergosterol in the crystal structure of the NTD at pH 6 of this study with that of the full-length NCR1 solved by cryo-EM (14), the sterol position differs. The ergosterol is bound ~4.5 Å deeper in the binding pocket of the crystal structure compared to the cryo-EM structures (Figure S2D). One explanation for this is that the crystal structure of the NTD represents a post-loading state, while the cryo-EM structures show the sterol approaching the transfer state (1).

The delipidated NTD did not crystallize, but crystals formed when C16 ceramide and edelfosine were added. Unfortunately, the data quality was not sufficient to confidently model these ligands, especially the long, flexible acyl chains that likely protrude from the binding pocket. However, these results prompted us to investigate the ability of the NTD to bind these compounds with biochemical assays. Previous *in vitro* assays have shown that the NTD from hNPC1 and hNPC2 can bind and transfer cholesterol and oxysterols (35,37,38). Binding assays show that yeast NPC2 binds cholesterol, ergosterol, dehydroergosterol (a fluorescent analog of ergosterol) and edelfosine (27), but also phospholipids and sphingolipids (28). This correlates with the larger binding pocket of NPC2 compared to human NPC2 (27). Here, it was assessed if the NTD binds the same NBD-labelled substrates as NPC2.

In general, the intensities measured for NPC2 binding to the substrates are higher than the intensities for the NTD binding to the corresponding compounds (Figure 3A and S3A). This could be caused by the NBD-group being in a more hydrophobic environment when bound by NPC2 compared the NTD. The reversal of substrate orientation from NPC2 to the NTD causes the NBD-group to be buried in the hydrophobic pocket of NPC2 (37). Since the fluorophore is attached to the hydrophobic tail of the lipid molecule, its binding to the NTD should be unperturbed, however, the NBD-group might protrude from the binding pocket of NTD and be partially exposed to the aqueous environment. The reversal of substrate orientation has only been observed for sterols and could be worth investigating with phospho- and sphingolipids.

The binding of NBD-PS and NBD-Cer to NPC2 is more than an order of magnitude stronger compared to that of the NTD (Table 1). Based on this strong interaction, it is unlikely that NPC2 will hand over these substrates to the NTD. It can thus be postulated that NPC2 acts as a general lipid solubilizer in the vacuole and might have other interaction partners (14). The order of K_D-values of NBD-Sph strongly indicates a favorable transfer of the substrate from NPC2 to the NTD since both proteins bind the substrate, but the affinity for binding by the NTD is stronger (Table 1). A higher affinity of the NTD towards a given lipid ligand compared to that of NPC2 could indicate directed lipid transfer from NPC2 to the NTD.

The concentrations of NBD-PC and NBD-PS used in the fluorescence binding experiments exceeded the CMC values previously determined to be 0.116 μM and 0.165 μM, respectively (44). It can be speculated that the concentration of 1 μM NBD-Cer, used in the binding assays, also exceeded the CMC of this lipid analogue. However, the CMC of NBD-Cer could not be measured since no discontinuity in the concentration-dependent fluorescence was found. In these cases, the determined K_D-values should be interpreted as apparent dissociation constants since the measured increase in fluorescence signal depends both on the binding equilibrium and the thermodynamics of micelle-to-monomer interconversion (28). In contrast, the concentrations of NBD-PI and NBD-Sph were lower

than the CMCs determined to be 2.3 μM and 12.0 μM (Figure S3A), respectively (44), therefore, the measured fluorescence intensities for these lipids were most likely not affected by micelle formation. This is relevant since significantly different K_D-values can be determined if measured above and below the CMC of a lipid probe as previously shown for NBD-PC (28). The K_D of NBD-PC binding to NPC2 is more than 100-fold smaller when the lipid concentration is below the CMC compared to above, but different photophysical mechanisms underlying the binding-induced fluorescence increase of NBD-lipids prevent a quantitative comparison of K_D values below and above their CMC (28). Thus, the K_D-values for binding of NBD-PC, NBD-PS and NBD-Cer to the proteins in this study cannot be directly compared to the K_D-values measured for NBD-PI and NBD-Sph, as for the latter lipids all binding studies were carried out with concentrations below their respective CMC. Only in this case, the binding model used provides direct estimates of K_D-values since no pre-equilibrium between lipid monomers and formed micelles exists. For all binding measurements above the analog's CMC, the measured K_D-values should be considered as apparent dissociation constants.

It cannot be ruled out that the NBD-moiety affects the properties of the lipid analogs used here and, therefore, the binding properties that were measured. To consolidate our findings, a different technique, based on the extraction of bi-functional pac-lipids from liposomes, was used. Among the selected pac-lipids, the NTD interacted mainly with cholesterol and sphingosine, in accordance with previous results in the mammalian NPC system (55), whereas NPC2 crosslinked with similar intensity with all tested ligands, suggesting a broader lipid binding function. These results correspond with the NBD-lipid assays, even though the crosslinking method is generally a more qualitative approach compared to fluorescence spectroscopy. The broad substrate scope of NPC2 could explain the more pronounced phenotypes in yeast when NPC2 is deleted, such as sterol accumulation, reduced vacuolar fusion, loss of raft-like domains in the limiting membrane and, ultimately, vacuolar fragmentation (27,56,57). Also, the smaller number and more severe phenotype of patients with defective hNPC2 compared to hNPC1 could point towards a higher lethality due to the involvement of hNPC2 in multiple lipid trafficking pathways (58).

When examining the effects of membrane composition on lipid binding, it seems that supplementing liposomes with excess ergosterol increased crosslinking of NPC2 with pacSph and, to a lesser extent, pac-Cer (Figure S7C and Figure S7D). This suggests a cooperative effect between ergosterol and sphingolipids in this *in vitro* setup. It can be speculated that the increased crosslinking with sphingolipid analogs could be caused by increased membrane recruitment and longer dwell time at sterol- and sphingolipid-enriched membrane regions (59). It was previously shown that sterol transfer by hNPC2 is slightly increased by ceramide and greatly promoted by lysobisphosphatidic acid (60,61). However, no noticeable effect of edelfosine on the crosslinking with individual pac-lipids were observed (Figure S7A and Figure S7B), possibly due to the low sensitivity of the crosslinking assay towards inhibitory effects.

The NTD from hNPC1 has been implicated in exporting lysosomal sphingosine (17,55). Here, the protein-to-protein transfer assay with photo-crosslinkable lipids revealed that pacSph was transferred from NPC2 to the NTD from yeast but not to STARD3, a sphingosine interactor from mammals (51, preprint). A recent study observed that NCR1 physically interacted with the ceramide synthase complex (62), which would be especially favorable for a rapid channeling of lysosomal sphingosine into ceramide synthesis, thus fueling transport along its concentration gradient. Attempts to perform this assay with pacCer in solution did not yield a positive result, possibly due to poor solubility of pacCer in buffer, which could prevent efficient loading of the His-tagged proteins (Figure S6).

In conclusion, the combination of X-ray crystallography and biophysics methods enable us to start uncovering the substrate scope of the NPC system from *S. cerevisiae*. We find that both NPC2 and the NTD interact with a wide range of structurally diverse lipids. Besides sterols, the yeast NPC system

seems capable of trafficking various lipids to the limiting membrane of vacuoles. Future efforts should be directed towards elucidating the relative kinetics of multiligand transfer by the NPC proteins in yeast, the regulation of such transport as well as the consequences of its defects on cellular growth and function.

ACKNOWLEDGEMENTS

We thank Prof. Bütikofer (University of Bern) for C6-NBD-PI. We recognize beamlines I24 and I04 at the Diamond Light Source and beamline BioMAX at the MAX IV Laboratory, where X-ray data were collected, and DESY-PETRA III for crystal screening. We acknowledge access to the computational infrastructure at the Center for Structural Biology at Aarhus University. We thank Julian Funk at Heidelberg University, for technical assistance.

This work was supported by the Danish Council for Independent Research (Grant Agreement No. 0135-00032B to BPP and 2032-00139B to DW), the Carlsberg Foundation (Grant Agreement No. CF19-0127), the European Research Council (Grant Agreement No. 637372) to BPP and the Deutsche Forschungsgemeinschaft (DFG, German Research Foundation, project number JA 3315/1-1 to DJ and project number 278001972 – TRR 186 to DH).

AUTHOR CONTRIBUTIONS

L Nel: purification of protein for biochemical assays, processing of structural data, building and analysis of structures, validation and deposition of structures, writing of the manuscript – original draft, editing and figures.

D Jamecna: conducting pac-lipid assays, writing of the manuscript – original draft, editing and figures.

K Thaysen: conducting NBD-substrate assays, writing of the manuscript – original draft, editing and figures.

E Olesen: purification of protein for structural studies and biophysics assays, collect and process X-ray crystallography data, initial building and analysis of structures, reading the manuscript.

M Szomek: conducting NBD-substrate assays.

J Langer: conducting pac-lipid assays.

K M Frain: purification of protein for biophysics assays.

D Höglinger: conceptualization, design of pac-lipid assays. Data analysis and writing of the manuscript.

D Wüstner: conceptualization, design of NBD-substrate assays. Data analysis and writing of the manuscript.

B P Pedersen: conceptualization, experimental design, validation and deposition of structures. Data analysis and writing of the manuscript.

CONFLICT OF INTEREST

The authors declare that they have no conflict of interest.

DATA AVAILABILITY

Atomic models and experimental maps have been deposited in the Protein Data Bank (PDB).

NTD with ergosterol: PDB 9F40. Raw data available at XRDa as XRD-00255.

NTD with cholesterol: PDB 9F41. Raw data available at XRDa as XRD-00256.

REFERENCES

1. Winkler MBL, Nel L, Frain KM, Dedic E, Olesen E, Pedersen BP (2022) Sterol uptake by the npc system in eukaryotes: A saccharomyces cerevisiae perspective. *FEBS Lett* 596: 160-179. doi:10.1002/1873-3468.14253
2. Krause MR, Regen SL (2014) The structural role of cholesterol in cell membranes: From condensed bilayers to lipid rafts. *Acc Chem Res* 47: 3512-3521. doi:10.1021/ar500260t
3. Schade DS, Shey L, Eaton RP (2020) Cholesterol review: A metabolically important molecule. *Endocr Pract* 26: 1514-1523. doi:10.4158/EP-2020-0347
4. Meng Y, Heybrock S, Neculai D, Saftig P (2020) Cholesterol handling in lysosomes and beyond. *Trends Cell Biol* 30: 452-466. doi:10.1016/j.tcb.2020.02.007

5. Kohler V, Aufschnaiter A, Buttner S (2020) Closing the gap: Membrane contact sites in the regulation of autophagy. *Cells* 9: doi:10.3390/cells9051184
6. Li SC, Kane PM (2009) The yeast lysosome-like vacuole: Endpoint and crossroads. *Biochim Biophys Acta* 1793: 650-663. doi:10.1016/j.bbamcr.2008.08.003
7. Hecht KA, O'Donnell AF, Brodsky JL (2014) The proteolytic landscape of the yeast vacuole. *Cell Logist* 4: e28023. doi:10.4161/cl.28023
8. Tan X, Li K, Wang Z, Zhu K, Tan X, Cao J (2019) A review of plant vacuoles: Formation, located proteins, and functions. *Plants (Basel)* 8: doi:10.3390/plants8090327
9. Trivedi PC, Bartlett JJ, Pulinilkunnil T (2020) Lysosomal biology and function: Modern view of cellular debris bin. *Cells* 9: doi:10.3390/cells9051131
10. Schrick K, Fujioka S, Takatsuto S, Stierhof YD, Stransky H, Yoshida S, Jurgens G (2004) A link between sterol biosynthesis, the cell wall, and cellulose in arabidopsis. *Plant J* 38: 227-243. doi:10.1111/j.1365-313X.2004.02039.x
11. Graef M (2018) Lipid droplet-mediated lipid and protein homeostasis in budding yeast. *FEBS Lett* 592: 1291-1303. doi:10.1002/1873-3468.12996
12. Neiss WF (1984) A coat of glycoconjugates on the inner surface of the lysosomal membrane in the rat kidney. *Histochemistry* 80: 603-608.
13. Ira Mellman RF, Ari Helenius (1986) Acidification of the endocytic and exocytic pathways. *Ann Rev Biochem*: 663-700.
14. Frain KM, Dedic E, Nel L, Bohush A, Olesen E, Thaysen K, Wustner D, Stokes DL, Pedersen BP (2024) Conformational changes in the niemann-pick type c1 protein ncr1 drive sterol translocation. *Proc Natl Acad Sci U S A* 121: e2315575121. doi:10.1073/pnas.2315575121
15. Peters C, Von Figura K (1994) Biogenesis of lysosomal membranes. *FEBS Lett* 346: 108-114. doi:10.1016/0014-5793(94)00499-4
16. Schroder BA, Wrocklage C, Hasilik A, Saftig P (2010) The proteome of lysosomes. *Proteomics* 10: 4053-4076. doi:10.1002/pmic.201000196
17. Lloyd-Evans E, Morgan AJ, He X, Smith DA, Elliot-Smith E, Sillence DJ, Churchill GC, Schuchman EH, Galione A, Platt FM (2008) Niemann-pick disease type c1 is a sphingosine storage disease that causes deregulation of lysosomal calcium. *Nat Med* 14: 1247-1255. doi:10.1038/nm.1876
18. Blom TS, Linder MD, Snow K, Pihko H, Hess MW, Jokitalo E, Veckman V, Syvanen AC, Ikonen E (2003) Defective endocytic trafficking of npc1 and npc2 underlying infantile niemann-pick type c disease. *Hum Mol Genet* 12: 257-272. doi:10.1093/hmg/ddg025
19. Hammond N, Munkacsi AB, Sturley SL (2019) The complexity of a monogenic neurodegenerative disease: More than two decades of therapeutic driven research into niemann-pick type c disease. *Biochim Biophys Acta Mol Cell Biol Lipids* 1864: 1109-1123. doi:10.1016/j.bbalip.2019.04.002
20. Subramanian K, Balch WE (2008) Npc1/npc2 function as a tag team duo to mobilize cholesterol. *Proc Natl Acad Sci U S A* 105:
21. Pfeffer SR (2019) Npc intracellular cholesterol transporter 1 (npc1)-mediated cholesterol export from lysosomes. *J Biol Chem* 294: 1706-1709. doi:10.1074/jbc.TM118.004165
22. Qian H, Wu X, Du X, Yao X, Zhao X, Lee J, Yang H, Yan N (2020) Structural basis of low-ph-dependent lysosomal cholesterol egress by npc1 and npc2. *Cell* 182: 98-111 e118. doi:10.1016/j.cell.2020.05.020
23. Berger AC, Vanderford TH, Gernert KM, Nichols JW, Faundez V, Corbett AH (2005) Saccharomyces cerevisiae npc2p is a functionally conserved homologue of the human niemann-pick disease type c 2 protein, hnpc2. *Eukaryot Cell* 4: 1851-1862. doi:10.1128/EC.4.11.1851-1862.2005
24. Malathi K, Higaki K, Tinkelenberg AH, Balderes DA, Almanzar-Paramio D, Wilcox LJ, Erdeniz N, Redican F, Padamsee M, Liu Y, et al (2004) Mutagenesis of the putative sterol-sensing domain of yeast niemann pick c-related protein reveals a primordial role in subcellular sphingolipid distribution. *J Cell Biol* 164: 547-556. doi:10.1083/jcb.200310046
25. Friedland N, Liou H-L, Lobel P, Stock AM (2003) Structure of a cholesterol-binding protein deficient in niemann–pick type c2 disease. *PNAS* 100: 2512-2517. doi:10.1073/pnas.0437840100

26. Xu S, Benoff B, Liou HL, Lobel P, Stock AM (2007) Structural basis of sterol binding by npc2, a lysosomal protein deficient in niemann-pick type c2 disease. *J Biol Chem* 282: 23525-23531. doi:10.1074/jbc.M703848200
27. Winkler MBL, Kidmose RT, Szomek M, Thaysen K, Rawson S, Muench SP, Wustner D, Pedersen BP (2019) Structural insight into eukaryotic sterol transport through niemann-pick type c proteins. *Cell* 179: 485-497 e418. doi:10.1016/j.cell.2019.08.038
28. Moesgaard L, Petersen D, Szomek M, Reinholdt P, Winkler MBL, Frain KM, Muller P, Pedersen BP, Kongsted J, Wustner D (2020) Mechanistic insight into lipid binding to yeast niemann pick type c2 protein. *Biochemistry* 59: 4407-4420. doi:10.1021/acs.biochem.0c00574
29. Gong X, Qian H, Zhou X, Wu J, Wan T, Cao P, Huang W, Zhao X, Wang X, Wang P, et al (2016) Structural insights into the niemann-pick c1 (npc1)-mediated cholesterol transfer and ebola infection. *Cell* 165: 1467-1478. doi:10.1016/j.cell.2016.05.022
30. Long T, Qi X, Hassan A, Liang Q, De Brabander JK, Li X (2020) Structural basis for itraconazole-mediated npc1 inhibition. *Nat Commun* 11: 152. doi:10.1038/s41467-019-13917-5
31. Tseng TT-T, Gratwick KS, Kollman J, Park D, Nies DH, Goffeau A, Saier MH (1999) The rnd permease superfamily: An ancient, ubiquitous and diverse family that includes human disease and development proteins. *J Mol Microbiol Biotechnol* 1:
32. Nikaido H (2018) Rnd transporters in the living world. *Res Microbiol* 169: 363-371. doi:10.1016/j.resmic.2018.03.001
33. Kwon HJ, Abi-Mosleh L, Wang ML, Deisenhofer J, Goldstein JL, Brown MS, Infante RE (2009) Structure of n-terminal domain of npc1 reveals distinct subdomains for binding and transfer of cholesterol. *Cell* 137: 1213-1224. doi:10.1016/j.cell.2009.03.049
34. Wang ML, Motamed M, Infante RE, Abi-Mosleh L, Kwon HJ, Brown MS, Goldstein JL (2010) Identification of surface residues on niemann-pick c2 essential for hydrophobic handoff of cholesterol to npc1 in lysosomes. *Cell Metab* 12: 166-173. doi:10.1016/j.cmet.2010.05.016
35. Infante RE, Abi-Mosleh L, Radhakrishnan A, Dale JD, Brown MS, Goldstein JL (2008) Purified npc1 protein. I. Binding of cholesterol and oxysterols to a 1278-amino acid membrane protein. *J Biol Chem* 283: 1052-1063. doi:10.1074/jbc.M707943200
36. Liou HL, Dixit SS, Xu S, Tint GS, Stock AM, Lobel P (2006) Npc2, the protein deficient in niemann-pick c2 disease, consists of multiple glycoforms that bind a variety of sterols. *J Biol Chem* 281: 36710-36723. doi:10.1074/jbc.M608743200
37. Infante RE, Radhakrishnan A, Abi-Mosleh L, Kinch LN, Wang ML, Grishin NV, Goldstein JL, Brown MS (2008) Purified npc1 protein: Ii. Localization of sterol binding to a 240-amino acid soluble luminal loop. *J Biol Chem* 283: 1064-1075. doi:10.1074/jbc.M707944200
38. Petersen D, Reinholdt P, Szomek M, Hansen SK, Poongavanam V, Dupont A, Heegaard CW, Krishnan K, Fujiwara H, Covey DF, et al (2020) Binding and intracellular transport of 25-hydroxycholesterol by niemann-pick c2 protein. *Biochim Biophys Acta Biomembr* 1862: 183063. doi:10.1016/j.bbamem.2019.183063
39. Frolov A, Zielinski SE, Crowley JR, Dudley-Rucker N, Schaffer JE, Ory DS (2003) Npc1 and npc2 regulate cellular cholesterol homeostasis through generation of low density lipoprotein cholesterol-derived oxysterols. *J Biol Chem* 278: 25517-25525. doi:10.1074/jbc.M302588200
40. McCauliff LA, Langan A, Li R, Ilnytska O, Bose D, Waghalter M, Lai K, Kahn PC, Storch J (2019) Intracellular cholesterol trafficking is dependent upon npc2 interaction with lysobisphosphatidic acid. *Elife* 8: doi:10.7554/eLife.50832
41. Berger AC, Hanson PK, Wylie Nichols J, Corbett AH (2005) A yeast model system for functional analysis of the niemann-pick type c protein 1 homolog, ncr1p. *Traffic* 6: 907-917. doi:10.1111/j.1600-0854.2005.00327.x
42. Revie NM, Iyer KR, Maxson ME, Zhang J, Yan S, Fernandes CM, Meyer KJ, Chen X, Skulska I, Fogal M, et al (2022) Targeting fungal membrane homeostasis with imidazopyrazoindoles impairs azole resistance and biofilm formation. *Nat Commun* 13: 3634. doi:10.1038/s41467-022-31308-1
43. Lu F, Liang Q, Abi-Mosleh L, Das A, De Brabander JK, Goldstein JL, Brown MS (2015) Identification of npc1 as the target of u18666a, an inhibitor of lysosomal cholesterol export and ebola infection. *Elife* 4: doi:10.7554/eLife.12177

44. Wüstner D, Herrmann A, Müller P (2000) Head group-independent interaction of phospholipids with bile salts: A fluorescence and epr study. *Journal of Lipid Research* 41: 395-404. doi:10.1016/s0022-2275(20)34478-3
45. Haberkant P, Stein F, Hoglinger D, Gerl MJ, Brugger B, Van Veldhoven PP, Krijgsveld J, Gavin AC, Schultz C (2016) Bifunctional sphingosine for cell-based analysis of protein-sphingolipid interactions. *ACS Chem Biol* 11: 222-230. doi:10.1021/acschembio.5b00810
46. Jamecna D, Hoglinger D (2024) The use of click chemistry in sphingolipid research. *J Cell Sci* 137: doi:10.1242/jcs.261388
47. Sasaki H, Arai H, Cocco MJ, White SH (2009) Ph dependence of sphingosine aggregation. *Biophys J* 96: 2727-2733. doi:10.1016/j.bpj.2008.12.3926
48. Demchenko AP, Mely Y, Duportail G, Klymchenko AS (2009) Monitoring biophysical properties of lipid membranes by environment-sensitive fluorescent probes. *Biophys J* 96: 3461-3470. doi:10.1016/j.bpj.2009.02.012
49. Shvadchak VV, Kucherak O, Afitska K, Dziuba D, Yushchenko DA (2017) Environmentally sensitive probes for monitoring protein-membrane interactions at nanomolar concentrations. *Biochim Biophys Acta Biomembr* 1859: 852-859. doi:10.1016/j.bbamem.2017.01.021
50. Dos Santos Rodrigues FH, Delgado GG, Santana da Costa T, Tasic L (2023) Applications of fluorescence spectroscopy in protein conformational changes and intermolecular contacts. *BBA Adv* 3: 100091. doi:10.1016/j.bbadva.2023.100091
51. Hempelmann P, Lolicato F, Graziadei A, Brown RDR, Spiegel S, Rappsilber J, Nickel W, Hoglinger D, Jamecna D (2023) The sterol transporter stard3 transports sphingosine at er-lysosome contact sites. *bioRxiv*: doi:10.1101/2023.09.18.557036
52. Klionsky DJ (1990) The fungal vacuole: Composition, function, and biogenesis. *Microb Rev* 54: 266-292. doi:10.1128/mr.54.3.266-292.1990
53. Van Ho A, Ward DM, Kaplan J (2002) Transition metal transport in yeast. *Annu Rev Microbiol* 56: 237-261. doi:10.1146/annurev.micro.56.012302.160847
54. Aufschnaiter A, Buttner S (2019) The vacuolar shapes of ageing: From function to morphology. *Biochim Biophys Acta Mol Cell Res* 1866: 957-970. doi:10.1016/j.bbamcr.2019.02.011
55. Altuzar J, Notbohm J, Stein F, Haberkant P, Hempelmann P, Heybrock S, Worsch J, Saftig P, Hoglinger D (2023) Lysosome-targeted multifunctional lipid probes reveal the sterol transporter npc1 as a sphingosine interactor. *Proc Natl Acad Sci U S A* 120: e2213886120. doi:10.1073/pnas.2213886120
56. Tsuji T, Fujimoto M, Tatematsu T, Cheng J, Orii M, Takatori S, Fujimoto T (2017) Niemann-pick type c proteins promote microautophagy by expanding raft-like membrane domains in the yeast vacuole. *Elife* 6: doi:10.7554/eLife.25960
57. Egebjerg JM, Szomek M, Thaysen K, Juhl AD, Kozakijevic S, Werner S, Pratsch C, Schneider G, Kapishnikov S, Ekman A, et al (2024) Automated quantification of vacuole fusion and lipophagy in saccharomyces cerevisiae from fluorescence and cryo-soft x-ray microscopy data using deep learning. *Autophagy* 20: 902-922. doi:10.1080/15548627.2023.2270378
58. Las Heras M, Szenfeld B, Ballout RA, Buratti E, Zanlungo S, Dardis A, Klein AD (2023) Understanding the phenotypic variability in niemann-pick disease type c (npc): A need for precision medicine. *NPJ Genom Med* 8: 21. doi:10.1038/s41525-023-00365-w
59. Lasserre R, Guo XJ, Conchonaud F, Hamon Y, Hawchar O, Bernard AM, Soudja SM, Lenne PF, Rigneault H, Olive D, et al (2008) Raft nanodomains contribute to akt/pkb plasma membrane recruitment and activation. *Nat Chem Biol* 4: 538-547. doi:10.1038/nchembio.103
60. Abdul-Hammed M, Breiden B, Adebayo MA, Babalola JO, Schwarzmann G, Sandhoff K (2010) Role of endosomal membrane lipids and npc2 in cholesterol transfer and membrane fusion. *J Lipid Res* 51: 1747-1760. doi:10.1194/jlr.M003822
61. McCauliff LA, Xu Z, Li R, Kodukula S, Ko DC, Scott MP, Kahn PC, Storch J (2015) Multiple surface regions on the niemann-pick c2 protein facilitate intracellular cholesterol transport. *J Biol Chem* 290: 27321-27331. doi:10.1074/jbc.M115.667469
62. Hammond N, Snider J, Stagljar I, Mitchell K, Lagutin K, Jessulat M, Babu M, Teesdale-Spittle PH, Sheridan JP, Sturley SL, et al (2023) Identification and characterization of protein interactions with the major niemann-pick type c disease protein in yeast reveals pathways of therapeutic potential. *Genetics* 225: doi:10.1093/genetics/iyad129

63. Mumberg D, Müller R, Funk M (1994) Regulatable promoters of saccharomyces cerevisiae: Comparison of transcriptional activity and their use for heterologous expression. *Nucleic Acids Res* 22: 5767-5768. doi:10.1093/nar/22.25.5767
64. Lyons JA, Shahsavar A, Paulsen PA, Pedersen BP, Nissen P (2016) Expression strategies for structural studies of eukaryotic membrane proteins. *Curr Opin Struct Biol* 38: 137-144. doi:10.1016/j.sbi.2016.06.011
65. Trimble RB, Tarentino AL (1991) Identification of distinct endoglycosidase (endo) activities in flavobacterium meningosepticum: Endo f1, endo f2, and endo f3. Endo f1 and endo h hydrolyze only high mannose and hybrid glycans. *Journal of Biological Chemistry* 266: 1646-1651. doi:10.1016/s0021-9258(18)52343-7
66. Hägglund P, Matthiesen R, Elortza F, Højrup P, Roepstorff P, Jensen ON, Bunkenborg J (2007) An enzymatic deglycosylation scheme enabling identification of core fucosylated n-glycans and o-glycosylation site mapping of human plasma proteins. *J Proteome Res* 6: 3021-3031. doi:10.1021/pr0700605
67. Adams PD, Afonine PV, Bunkoczi G, Chen VB, Davis IW, Echols N, Headd JJ, Hung LW, Kapral GJ, Grosse-Kunstleve RW, et al (2010) Phenix: A comprehensive python-based system for macromolecular structure solution. *Acta Crystallogr D Biol Crystallogr* 66: 213-221. doi:10.1107/S0907444909052925
68. Liebschner D, Afonine PV, Baker ML, Bunkoczi G, Chen VB, Croll TI, Hintze B, Hung LW, Jain S, McCoy AJ, et al (2019) Macromolecular structure determination using x-rays, neutrons and electrons: Recent developments in phenix. *Acta Crystallogr D Struct Biol* 75: 861-877. doi:10.1107/S2059798319011471
69. Sparta KM, Krug M, Heinemann U, Mueller U, Weiss MS (2016) Xdsapp2.0. *Journal of Applied Crystallography* 49: 1085-1092. doi:10.1107/s1600576716004416
70. Emsley P, Lohkamp B, Scott WG, Cowtan K (2010) Features and development of coot. *Acta Crystallogr D Biol Crystallogr* 66: 486-501. doi:10.1107/S0907444910007493
71. Chen VB, Arendall WB, 3rd, Headd JJ, Keedy DA, Immormino RM, Kapral GJ, Murray LW, Richardson JS, Richardson DC (2010) Molprobity: All-atom structure validation for macromolecular crystallography. *Acta Crystallogr D Biol Crystallogr* 66: 12-21. doi:10.1107/S0907444909042073
72. Young JY, Westbrook JD, Feng Z, Sala R, Peisach E, Oldfield TJ, Sen S, Gutmanas A, Armstrong DR, Berrisford JM, et al (2017) Onedep: Unified wwpdb system for deposition, biocuration, and validation of macromolecular structures in the pdb archive. *Structure* 25: 536-545. doi:10.1016/j.str.2017.01.004
73. Kurisu G, Bekker GJ, Nakagawa A (2022) History of protein data bank japan: Standing at the beginning of the age of structural genomics. *Biophys Rev* 14: 1233-1238. doi:10.1007/s12551-022-01021-w
74. Pettersen EF, Goddard TD, Huang CC, Meng EC, Couch GS, Croll TI, Morris JH, Ferrin TE (2021) Ucsf chimerax: Structure visualization for researchers, educators, and developers. *Protein Sci* 30: 70-82. doi:10.1002/pro.3943
75. Stourac J, Vavra O, Kokkonen P, Filipovic J, Pinto G, Brezovsky J, Damborsky J, Bednar D (2019) Caver web 1.0: Identification of tunnels and channels in proteins and analysis of ligand transport. *Nucleic Acids Res* 47: W414-W422. doi:10.1093/nar/gkz378

MATERIAL & METHODS

Yeast cultivation and expression of the NTD

The DNA sequence of the N-terminal domain of NCR1 (residue 1 to 249, UniProt: Q12200) was introduced into an expression construct based on p423-GAL1, with a C-terminal thrombin cleavage site and a deca-histidine tag for purification (63). Transformed *S. cerevisiae* (strain DSY-5, Gentaur) was grown in baffled shaker flasks for 30 h and harvested after a 22 h induction using galactose (64). Harvested cells were washed in cold water, spun down and stored at -80°C.

Purification of the NTD for crystallization and assays

Cells were thawed in lysis buffer (600 mM NaCl, 100 mM Tris-HCl pH 7.5) supplemented with 1.2 mM PMSF, while gently stirring for 30 min. The cells were lysed by agitation with 0.5 mm glass beads (Biospec Products). The cell lysate was removed from the glass beads by filtering and then centrifuged at 9,000 rpm at 4°C for 20 min to pellet cell debris. The cell-free extract was ultracentrifuged at 42,000 rpm at 4°C for 1 h to pellet membranes and cell debris. The supernatant was filtered and loaded onto a 5 mL IMAC Ni-NTA HP column (Cytiva) pre-equilibrated with Wash buffer [500 mM NaCl, 10% (v/v) glycerol, 20 mM imidazole, 50 mM Tris-HCl pH 7.5]. Next, contaminant proteins were washed away with 50 mL of W70 buffer (Wash buffer with 70 mM imidazole).

If endogenous lipid was retained, 45 mL of G20 buffer (200 mM NaCl, 20 mM imidazole, 20 mM Tris-HCl pH 7.5) was passed through the column and 175 units of thrombin (Avantor) were added to 5 mL of G20 to circulate over the column at 4°C, overnight. Since the HisTag had been cleaved off, the NTD was eluted with 15 mL G40 buffer (200 mM NaCl, 40 mM imidazole, 20 mM Tris-HCl pH 7.5) and was concentrated to < 500 µL in a 20 mL 10 kDa MWCO concentrator (Satorius Vivaspin). Aggregates were removed by filtering the concentrated sample with a 0.22 µm PVDF membrane spin-column (Durapore, Merck). The flow-through was injected onto an S75 Increase 10/300 GL column (Cytiva), pre-equilibrated with G-buffer (150 mM NaCl and 20 mM MOPS pH 6.5). The peak fractions were pooled and concentrated with a 500 µL 10 kDa MWCO concentrator to 3.3 mg/mL for assays with NBD-lipids and 1 mg/mL for assays with pac-lipids.

If the endogenous lipid had to be removed, the same procedure as above applied but with two additional wash steps. Before the step of washing with G20 buffer, 100 mL of W70S buffer (W70 buffer supplemented with 100 mM methyl-β-cyclodextrin) was passed through the column, followed by 50 mL of W70 buffer, purified as described above and used in substrate-binding assays. For crystallography, the endogenous lipid was removed with methyl-β-cyclodextrin and exchanged with 50 mL of W70 buffer containing 50 µM lipid of choice, (cholesterol, ergosterol, C16 ceramide, or edelfosine), dissolved in 2 CMC of *n*-dodecyl-β-D-maltoside (DDM) detergent. The detergent was removed by washing with 100 mL of W70 buffer and the rest of the purification followed as described above.

Yeast cultivation and expression of NPC2

The gene of NPC2 (residue 1 to 173, UniProt: Q12408) was cloned into the same type of expression vector as described for the NTD. Cell growth and induction of homologous over-expressed protein were the same as for the NTD. Harvested cells were washed in cold water, spun down and stored at -80°C.

Purification of NPC2 for assays

The purification protocol for the NPC2 was identical to that of the NTD, except the G-buffer used for size-exclusion chromatography (200 mM NaCl, 20 mM Tris-HCl pH 7.5). To delipidate NPC2 with methyl-β-cyclodextrin, the same procedure applied as described for the NTD. The peak fractions

were pooled and concentrated with a 500 µL 10 kDa MWCO concentrator, either to 2.2 mg/mL or 1 mg/mL for biochemical assays with NBD-lipids and pac-lipids, respectively.

Deglycosylation of the NTD

0.5-5 mg/mL of enzyme and 1 mg/mL purified NTD were incubated on a rotating table at 4°C with one of five deglycosylases: PNGase F (hydrolyses the bond between asparagine and the first *N*-acetylgoucosamine), Endo H (hydrolyses the glycosidic linkage between the two core *N*-acetylgoucosamines), Endo F1 (cleaves hybrid but not complex oligosaccharides), Endo F2 (leaves one *N*-acetylglucosamine attached to asparagine) and Endo F3 (does not cleave high mannose or hybrid glycan chains) (65,66). For controls, the NTD without enzymes and the enzyme alone was also prepared. SDS-loading dye was added to the samples after 1 h, boiled for 1 min and visualized by SDS-PAGE.

NTD crystallography, data collection, processing and building

Purified NTD with either ergosterol or cholesterol bound were evaluated with crystallization screens. Conditions containing 20-300 mM $ZnSO_4$, 45-48% (v/v) PEG200 and MOPS/MES at pH 5.5-6.5 yielded crystals at 19°C and micro-seeding of the NTD at 8 mg/mL. Optimization of initial crystal hits was done in 50 mM ZnSO4, 42% PEG200 and 100 mM MES pH 6 with the addition of Hampton additive screen in 96-well plates. A Mosquito Robot (Mosquito Xtal3, SPT Labtech) was used to add 200 nL of the NTD at 16 mg/mL to 200 nL of mother liquor and the trays were incubated at 4°C. After eight days, crystals appeared and were left to keep growing. The NTD with ergosterol bound produced crystals with 4% (v/v) acetonitrile as additive and the NTD bound to cholesterol with 3% v/v 2-methyl-2,4-pentanediol (MPD) additive. Additional cryoprotectant was not added prior to freezing in liquid nitrogen.

Final datasets were collected at the MAXIV beamline (BioMAX) using an EIGER DECTRIS 16 M detector. XDSapp v3.1.9 was used to process the data and the NTD from NCR1 (PDB: 6R4L) was used for molecular replacement with the Phaser module in PHENIX v1.20 (67,68,69). Extensive glycosylation resulted in high solvent content and translational non-crystallographic symmetry. MR solutions were obtained in spacegroup 18 ($P2_122_1$). Iterative rounds of model building and refinement were done in Coot v0.9.8.7 (70) and phenix.refine, respectively. MolProbity statistics were used to guide model building (Table S1) (71). The final models and maps were validated and deposited on the PDB OneDep server (72) and raw data on XRDa (73).

Fluorescence binding assays

Fluorescence binding assays were conducted using NBD-PC, -PS, -Cer and -Sph (Avanti Polar Lipids) and NBD-PI (Prof. Bütikofer), dissolved in ethanol. A solution of 1 µM NBD-lipid in either MES buffer (200 mM NaCl, 50 mM MES pH 5.5) or Tris buffer (50 mM Tris pH 7.5) was transferred to 0.1 cm thick Quartz cuvettes. NBD-lipids were excited at 460 nm and the emission spectra were recorded within a range of 490 to 600 nm. Either the NTD or NPC2 were titrated in increasing concentrations to the sample cuvette. The sample solution, not exceeding 1% ethanol, was mixed with protein and incubated for 10 min. Measurements were conducted with an ISS Chronos spectrofluorometer (Urban-Champaign, IL) with 0.5 mm slit width and no polarization. Emission spectra for NBD-lipids were measured as a control and subtracted from the sample emission spectra. The control cuvette was measured every time the sample was measured to correct the data for bleaching of NBD-Sph.

For measuring the ability of edelfosine to outcompete NBD-Sph, 1 µM NBD-Sph and 1 µM NTD were mixed to form the interaction complex before adding increasing amounts of edelfosine. As a control, edelfosine was titrated into a cuvette containing exclusively NBD-Sph in buffer. To measure

the competitive binding between NBD-Sph and edelfosine, 1 µM NBD-lipid in Tris buffer was mixed with either 0.1, 0.5 or 0.7 µM edelfosine in the sample cuvette prior to titration with the NTD.

CMC measurements

The CMC of NBD-Sph was measured by adding increasing concentrations of NBD-Sph to a cuvette containing MES buffer. Between measurements, the solution was mixed and incubated for 10 min. The highest measured concentration of NBD-Sph was 30 µM.

As edelfosine is not fluorescent, a different approach was used to measure its CMC. The hydrophobic dye, Sudan Black B, was used to stain micelles. The absorption of solutions consisting of MES buffer, Sudan Black and increasing concentrations of edelfosine were measured using a spectrophotometer (Hitachi U-2010).

Analysis of spectroscopy data

Prior to determination of dissociation constants, the measurements were normalized. The protein-lipid binding measurements were normalized to the highest value in each dataset. For the competition assay, the data was normalized to the lowest value in the dataset to be able to fit all data to equation (1), the full model for one-site binding for the saturated fraction, *f* (27):

$$\frac{[RL]}{R_t} = \frac{R_t + K_d + L_t - \sqrt{(R_t + K_d + L_t)^2 - 4 \cdot R_t \cdot L_t}}{2 \cdot R_t} = f \tag{1}$$

Here, [RL] is the concentration of the receptor-ligand complex, R_t is the total concentration of the receptor and L_t is the concentration of the ligand. Since the protein is titrated, the lipids are acting as the receptor, whereas the protein counts as the ligand.

To determine the dissociation constant of edelfosine (referred to as K_I) in the competition assay, it can be assumed that the binding is simple and that all added ligand is bound. In this case, the IC50 can be used to calculate a K_I using equation (2) on normalized data:

$$K_i = IC50 \cdot \frac{K_d}{K_d + [L]} \tag{2}$$

The K_D is the dissociation constant of the ligand, [L] is the concentration and IC50 is the concentration of the inhibitor, where half of the ligand is inhibited.

To determine the CMC, the sigmoid curve was fitted and adjusted to the normalized data:

$$f(x) = \frac{l}{1 + e^{-k \cdot (x - x_0)}} + b \tag{3}$$

Here, l is the scaling of the y-axis, x_0 represents the CMC, k determines the sharpness of the fitted curve and b is the starting position on the y-axis.

Liposome preparation

Lipids from stock vials were dissolved in chloroform and mixed at the desired molar ratio. For *in vitro* crosslinking, most liposomes consisted of 88.5 mol% DOPC as carrier lipid, 10 mol% DOPS and 1.5 mol% respective pac-lipid. The pac-lipids were incorporated into liposomes at low

concentrations (1.5 mol%) to ensure homogenous distribution and avoid micelle formation. The solvent was evaporated in a rotary evaporator (Heidolph) for 30 min at 42°C at 150 rpm to create a thin lipid film. Lipid films were hydrated with filtered and degassed phosphate buffered saline (PBS; 137 mM NaCl, 2.7 mM KCl, 10 mM Na_2HPO_4, 1.8 mM KH_2PO_4 pH 7.4). Solutions of hydrated lipids (with total lipid concentration of 2 mM) were subjected to 5 freeze-thaw cycles in liquid nitrogen and warm water (42°C) to facilitate breakup of large structures and support formation of smaller multilamellar vesicles. Lipid solutions were stored at -20°C. Before use, liposomes were extruded by passing 20x through a 100 nm pore size polycarbonate filter (Whatman, Nucleopore) using a hand extruder (Avanti Polar Lipids). Extruded liposomes were stored at 4°C, protected from light and used within 1-2 days.

***In vitro* crosslinking assay**

Extruded liposomes were diluted in PBS until final lipid concentration of 60 µM, including 1 µM pac-lipid. Purified proteins were added until final concentration of 1.5 µM in a reaction volume of 100 µL. Protein-liposome mixtures were incubated in 0.5 mL Eppendorf tubes for 30 min at 37°C at 400 rpm, then crosslinked (or not) by exposure to 365 nm UV light for 15 min at 4°C using a 100 W mercury lamp (Blak-Ray B-100AP). After crosslinking, the click reaction was performed by adding 0.7 µL of freshly prepared click mix into the sample tubes. The final concentrations of click reagents in sample tubes were 80 µM $CuSO_4$ (Merck), 3 µM TBTA (Merck), 3 µM Picolyl-AF647-Azide (Jena Bioscience) and 80 µM ascorbic acid (Merck). Fresh stock of ascorbic acid solution in water was prepared every time and added to the click mix immediately before starting the click reaction. Click reactions were allowed to proceed for 2 h at 37°C at 400 rpm. Then, samples were concentrated in a vacuum evaporator for 30 min set to 30°C and supplemented with 4x Lämmli buffer (250 mM Tris pH 6.8, 9.2% SDS, 40% glycerol, 0.2% bromophenol blue, 100 mM DTT). Samples were boiled for 5 min at 95°C and clicked protein-lipid complexes were resolved by SDS-PAGE. After extensive destaining in a destain solution (65% water, 25% isopropanol and 10% acetic acid), the AF647 (a structural analog of Alexa Fluor® 647) and Coomassie images were acquired using the Licor Odyssey imaging system. Data were evaluated by subtracting background fluorescence, followed by comparing the AF647 signal between crosslinked and non-crosslinked samples, normalized to protein loading based on Coomassie staining. The resulting values are described as +UV/-UV ratios. Statistics were calculated with the Mann Whitney U test.

***In vitro* pacSph transfer assay**

Purified His-tagged proteins (5 µM of sfGFP, STARD3 or NPC2) were incubated with 10 µM pacSph in PBS for 60 min at 25°C at 500 rpm. Next, the His-tagged proteins were captured on NiNTA beads and washed 5x with PBS to remove unbound pacSph. NiNTA beads with bound proteins were then incubated with 2.5 µM of untagged NTD for 60 min at 25°C at 500 rpm. After removal of the beads, the NTD was subjected (or not) to UV-crosslinking. After crosslinking, the click reaction was performed as described above and samples were resolved on SDS-PAGE. For data analysis, background was subtracted and the +UV/-UV ratios were quantified for each sample as described previously. After that, the +UV/-UV ratio of sfGFP, incapable of binding sphingosine, was set as baseline (=1) to compare the pacSph transfer capability of STARD3 and NPC2 to the NTD. Statistics were calculated with the Mann Whitney U test.

Figure preparation

All figures were annotated in Inkscape and graphical representations of the structures were made in ChimeraX v1.71 (74). Graphs were created in GraphPad Prism 10 (San Diego, CA), while CaverWeb v1.2 (75) was used to obtain dimensions of the extended pocket.

MAIN TEXT FIGURES, TABLE AND LEGENDS

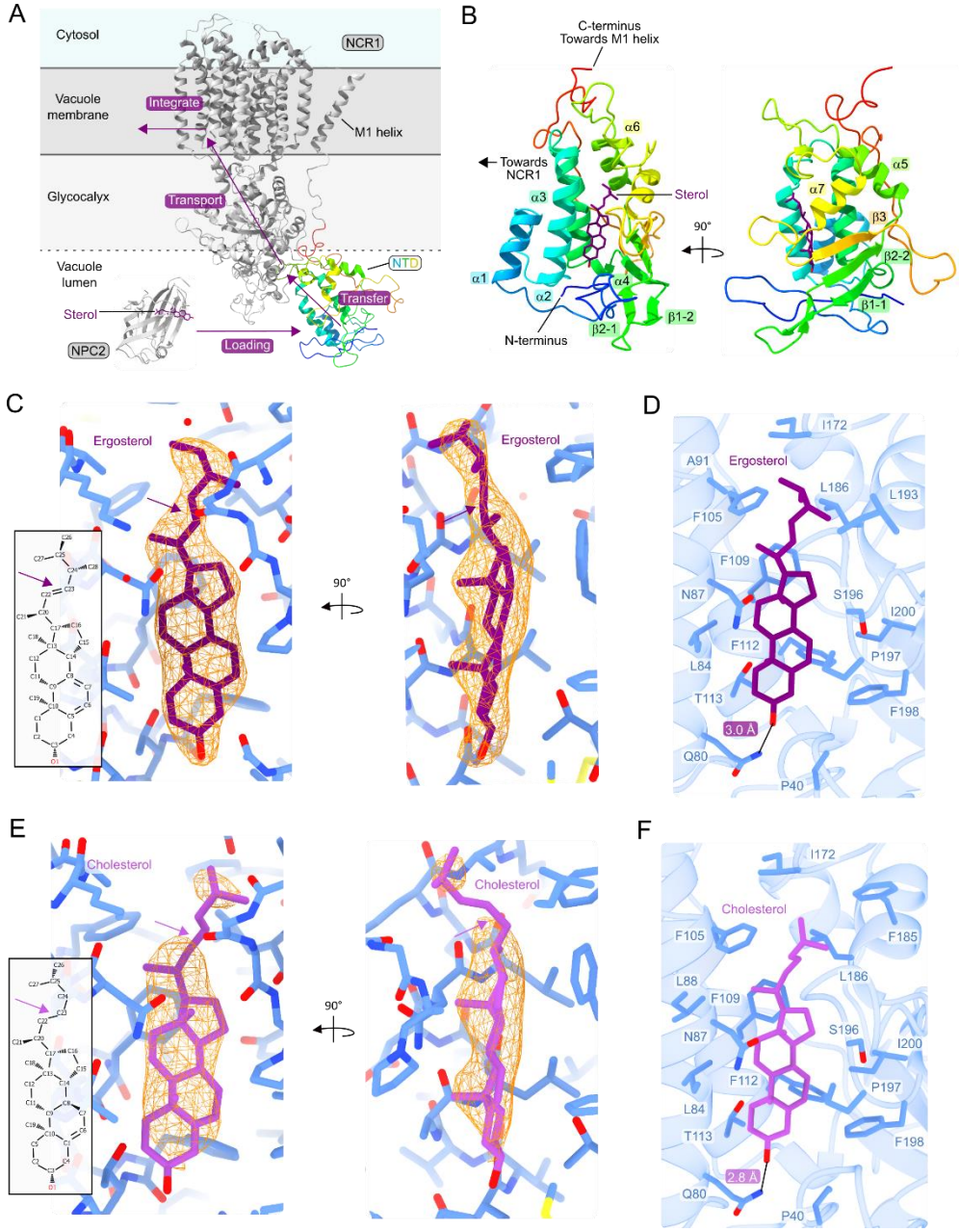

Figure 1. Structures of the NTD bound to sterols

(A) Structure of NCR1 (PDB ID: 6R4L) in grey with the NTD in color. NTD loading from NPC2 (PDB ID: 6R4N) is followed by transfer, transport and integration by NCR1 into the vacuole membrane. **(B)** Secondary structure elements of the NTD. **(C)** Chemical structure and density of ergosterol in the binding pocket of the NTD. **(D)** Residues surrounding ergosterol in the binding pocket of the NTD. **(E)** Chemical structure and density of cholesterol in the binding pocket of the NTD. **(F)** Residues surrounding cholesterol in the binding pocket of the NTD.

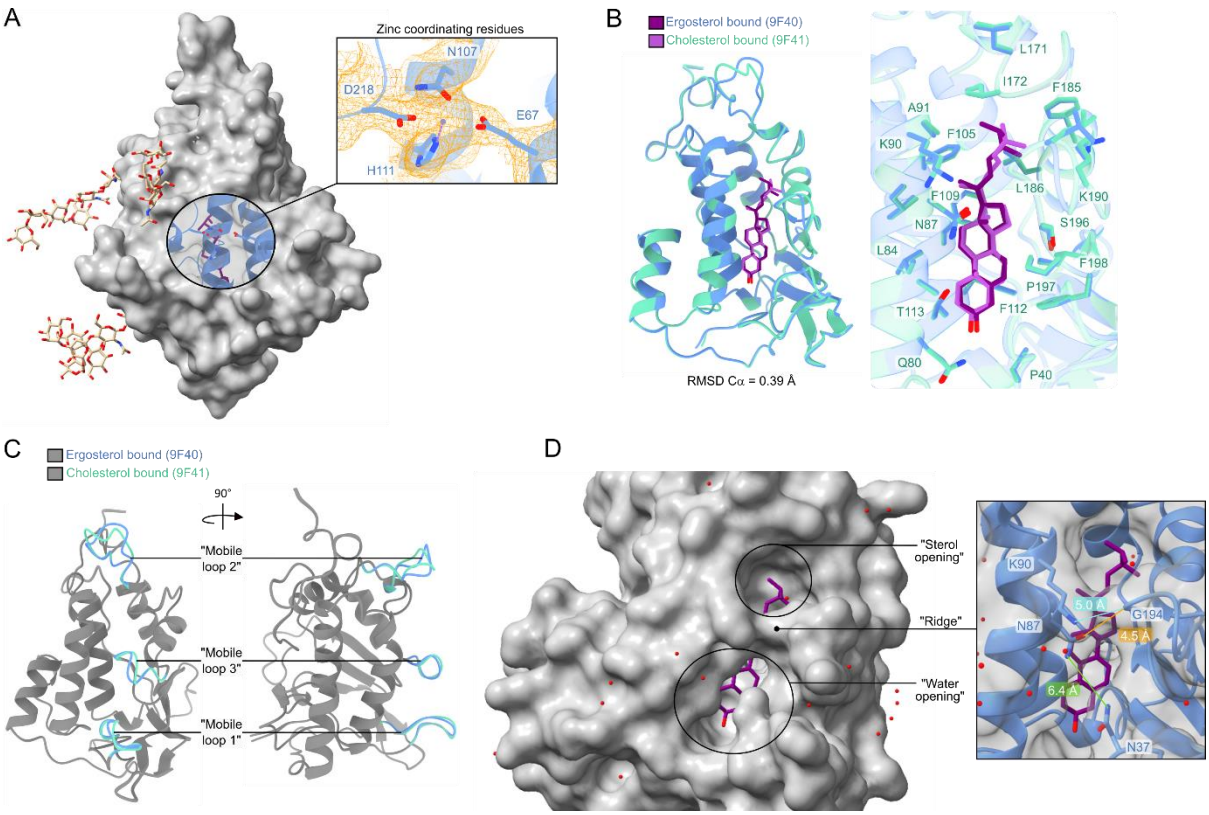

Figure 2. Structural features of the NTD

(A) Ion-coordinating residues at the back of the substrate binding pocket. **(B)** Superposition of NTD structures bound to ergosterol and cholesterol. The sterols and residues of both binding pockets are overlayed. **(C)** Three "mobile loops" with different positions when comparing the NTD bound to ergosterol and cholesterol. **(D)** Residues that form the "ridge" and that likely govern substrate accessibility to the binding pocket also divides the pocket into a "sterol-opening" and a "water-opening".

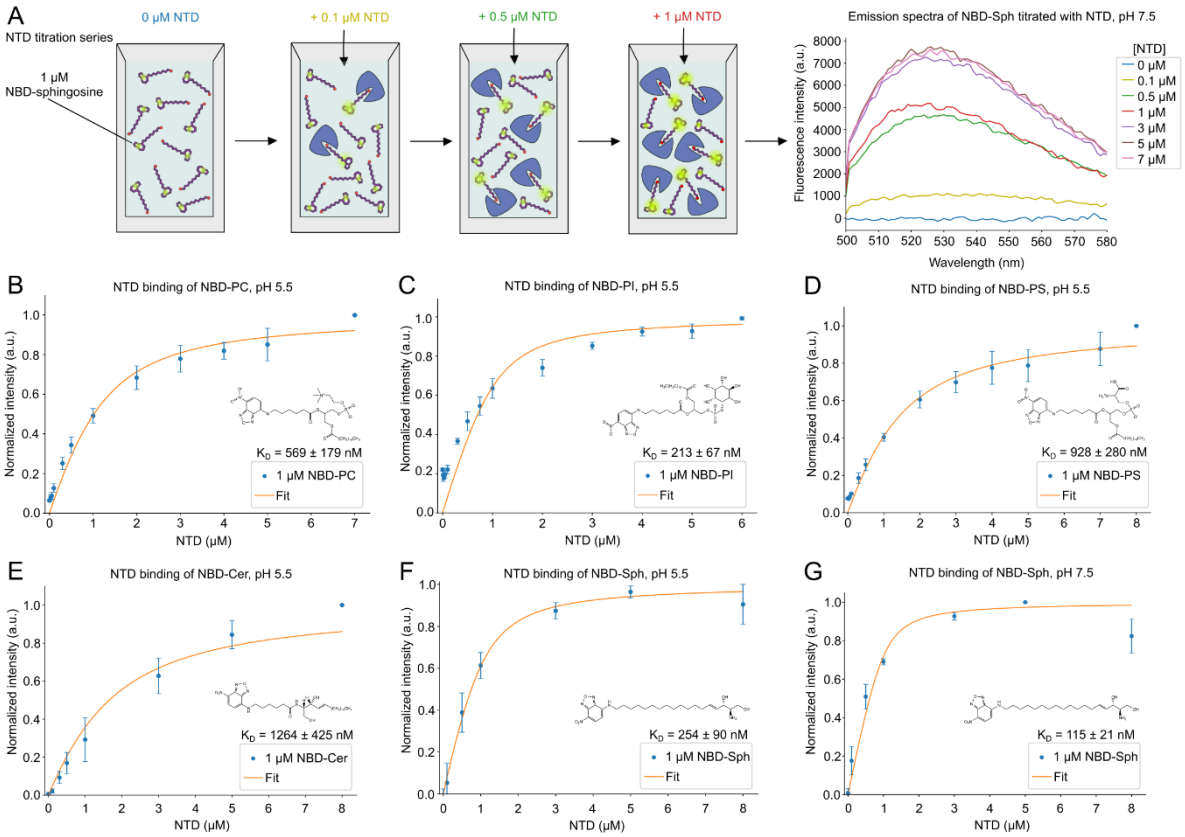

Figure 3. NTD binding to phospho- and sphingolipids

(A) An overview of the principle behind the fluorescence binding assay. The graph shows representative raw emission spectra in a range of 500 nm to 580 nm of NBD-Sphingosine (NBD-Sph), measured with varying concentrations of the NTD. The excitation wavelength was 460 nm. Measurements were conducted using a 1 µM NBD-Sph solution in 50 mM Tris (pH 7.5), while titrating increasing concentrations of the NTD. After addition of NTD, the solution was incubated for 10 min to ensure equilibrium was reached before the next measurement. **(B-E)** The fluorescence for NBD-phosphatidylcholine, NBD-phosphatidylinositol, NBD-phosphatidylserine and NBD-ceramide, respectively, are shown as a result of binding to increasing concentrations of NTD at pH 5.5. The measurements were conducted at an excitation wavelength of 460 nm and emission wavelength of 530 nm. For each lipid-protein complex a dissociation constant (K_D) is determined and shown in the corresponding graphs. Data points show mean ± standard error of mean (SEM) of three (n = 3) independent experiments. **(F, G)** Normalized fluorescent signal for NBD-Sph at an excitation wavelength of 460 nm and an emission wavelength of 530 nm show increasing fluorescence intensity as a result of binding to increasing concentrations of NTD at pH 5.5 **(F)** or pH 7.5 **(G)**. The K_D-values are determined and shown in the graphs. Data points show mean ± SEM of three (n = 3) independent experiments.

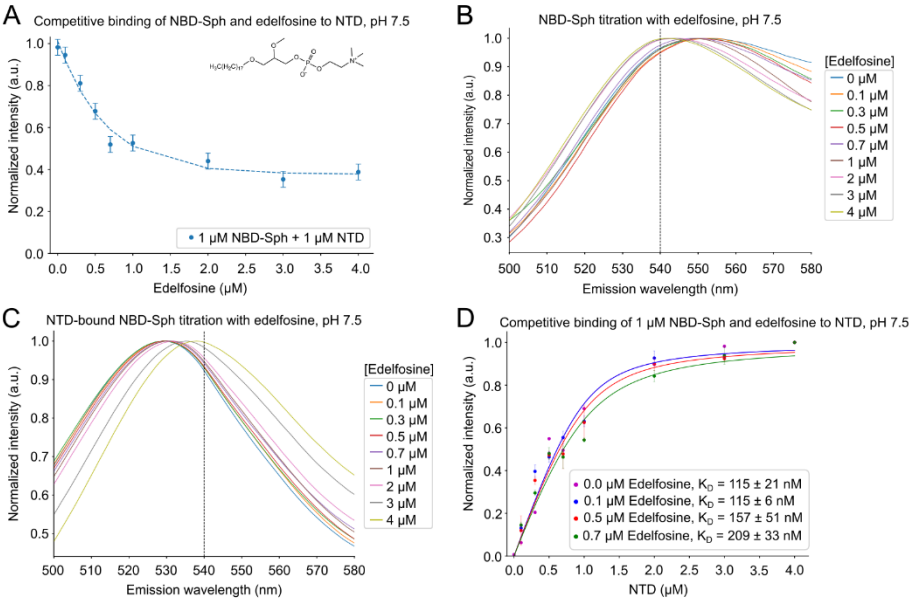

Figure 4. Competitive binding of edelfosine and sphingosine to the NTD

(A) Normalized fluorescence of 1 μM NBD-Sphingosine (NBD-Sph) mixed with 1 μM NTD, with concentrations ranging from 0 μM to 4 μM of edelfosine at pH 7.5. The excitation and emission wavelengths are 460 nm and 530 nm, respectively. The IC50 is estimated to be 0.5 μM. The data points show mean ± standard error of mean (SEM) of three (n = 3) independent experiments. **(B)** Each emission spectra of 1 μM NBD-Sph with varying edelfosine concentrations at pH 7.5 normalized to 1. The measurements were obtained using an excitation wavelength of 460 nm. The dashed line marks 540 nm. **(C)** Similar to **(B)** but with 1 μM NTD in the solution. **(D)** Normalized NBD-signal of 1 μM NBD-Sph incubated with either 0 (magenta), 0.1 (blue), 0.5 (red) or 0.7 (green) μM edelfosine at increasing concentrations of the NTD. The data points show mean ± SEM of three (n = 3) independent experiments in the presence of edelfosine, whereas the data points without edelfosine show the mean of two (n = 2) independent experiments.

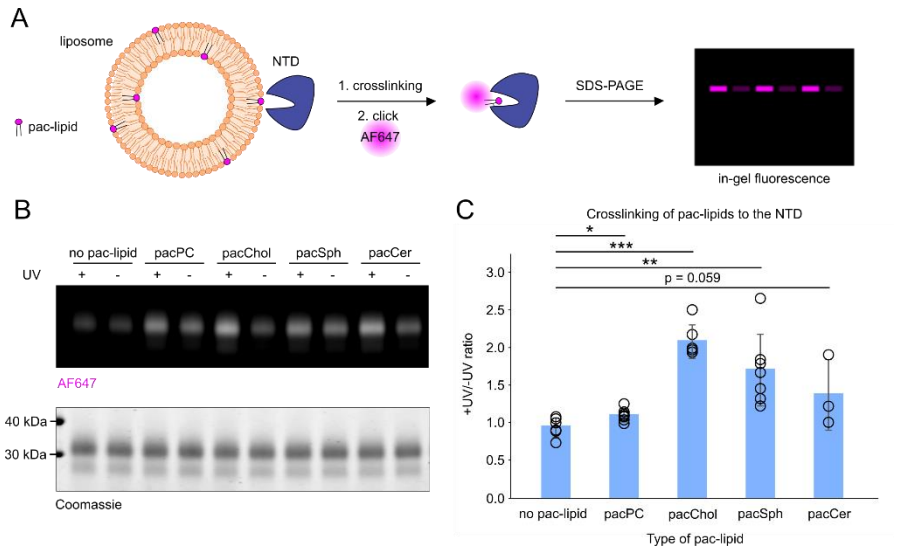

Figure 5. NTD crosslinking with pac-lipids

(A) Schematic illustration of liposome crosslinking assay performed for experiments shown in (B) and quantified in (C). **(B)** Representative gel image with crosslinking profile of purified NTD. Liposomes containing 1.5 mol% of indicated pac-lipids (1 µM pac-lipid) were incubated with 1.5 µM NTD and UV-crosslinked. Protein-lipid complexes were subjected to click reaction with AF647-picolyl azide and visualized by SDS-PAGE. In-gel fluorescence of AF647 was normalized to loaded protein in each well based on Coomassie staining. **(C)** Normalized in-gel fluorescence is quantified as +UV/-UV signal ratio. N = at least 4 independent experiments.

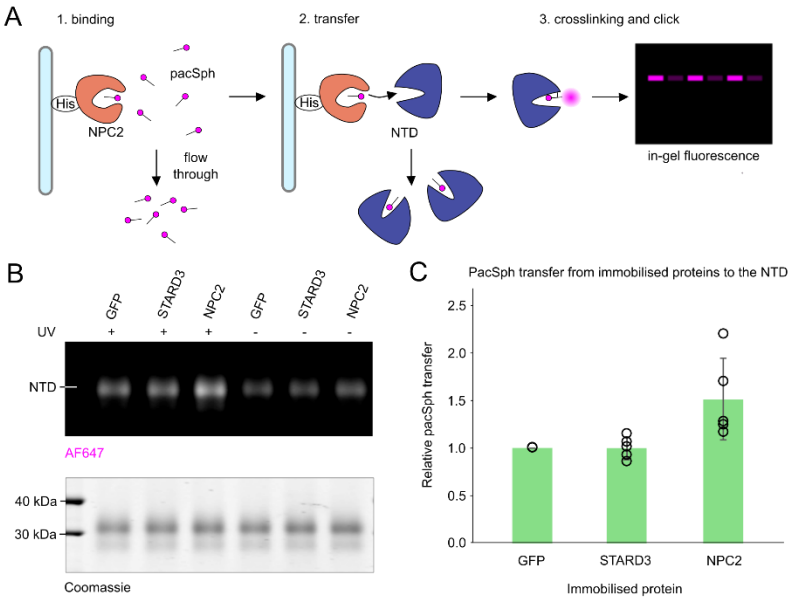

Figure 6. Pac-lipid transfer assay to the NTD

(A) Schematic illustration of pacSph transfer assay performed for experiments shown in (B) and quantified in (C). **(B)** Representative gel image showing the fluorescently labelled pacSph-NTD complexes. Soluble pacSph was incubated with His-tagged GFP (normalization control), STARD3 (negative control) or NPC2. Unbound pacSph was washed away and then His-tagged proteins were incubated with soluble untagged NTD. After 1 h of incubation, the NTD was subjected to UV crosslinking and click reaction with AF647. Crosslinked and stained protein-lipid complexes were resolved on SDS-PAGE. In-gel fluorescence of AF647 was first normalized to loaded protein. Then, +UV/-UV ratios were calculated. The +UV/-UV ratio of GFP was used as baseline (= value 1 for each experiment). **(C)** Quantification of normalized in-gel fluorescence. N = at least 5 independent experiments.

Table 1. Overview of K_D-values for lipid-protein complexes

Lipid	pH	Protein	K_D (nM)
NBD-C6-PC	5.5	NTD	569 ± 179°
		NPC2	492*°
NBD-C6-PI	5.5	NTD	213 ± 67
		NPC2	10*
NBD-C6-PS	5.5	NTD	928 ± 280°
		NPC2	16± 5°
NBD-C6-Cer	5.5	NTD	1264 ± 425°
		NPC2	91 ± 77°
NBD-Sph	5.5	NTD	254 ± 90
		NPC2	580 ± 154
NBD-Sph	7.5	NTD	115 ± 21
		NPC2	530 ± 166

Results from (28) indicated as *. Apparent K_D marked with °.

SUPPLEMENTAL FIGURES, TABLE AND LEGENDS

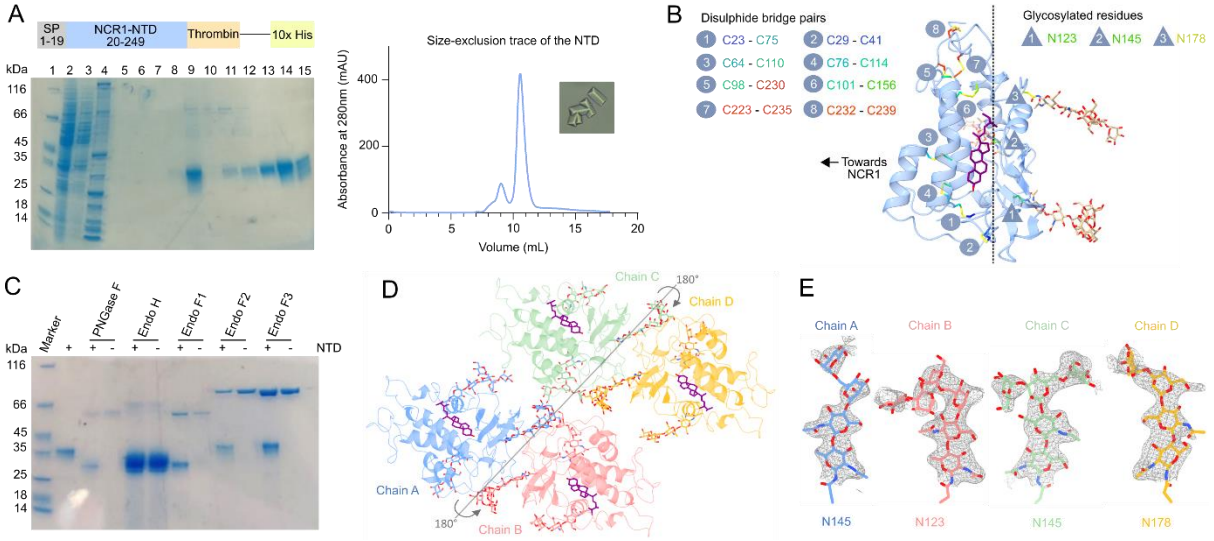

Figure S1. Purification and crystallization of the NTD with all N-glycosylation sites
(A) Construct containing the NTD, its purification by IMAC and SEC as well as representative crystals. Samples for SDS-PAGE were collected throughout the purification. Lane 1: marker, lane 2: IMAC load, lane 3: IMAC flow-through, lane 4: wash flow-through, lane 5: wash + β-cyclodextrin flow-through, lane 6: wash flow-through, lane 7: G20 flow-through, lane 8: G40 flow-through, lane 9: SEC load, lane 10: SEC fraction 2, lane 11: SEC fraction 3, lane 12: SEC fraction 4, lane 13: SEC fraction 6, lane 14: peak SEC fraction 7 and lane 15: SEC fraction 8. **(B)** Location of eight disulfide bridges and three N-glycosylated residues. **(C)** SDS-PAGE of the NTD treated with various deglycosylases. **(D)** Packing of four NTD monomers in the asymmetric unit. **(E)** Examples of density for glycan chains from each monomer in the asymmetric unit.

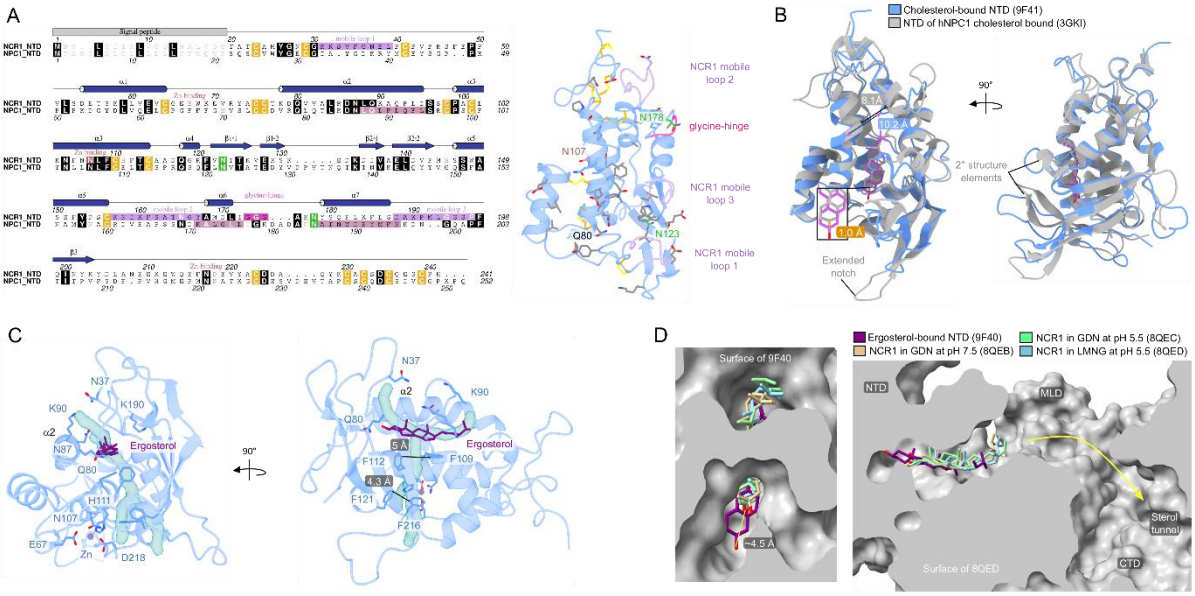

Figure S2. Comparison of the NTD with that of hNPC1 and full-length NCR1

(A) Sequence alignment of the NTD and the NTD of hNPC1. Secondary structure annotation is based on the NTD of NCR1. The model of the NTD is colored according to the alignment: conserved residues (grey), disulfide bridges (orange), N-glycosylated (green), mobile loops (light purple), glycine hinge (pink) and Zn-binding site (light brown). **(B)** Superposition of the NTD (PDB ID: 9F41) and the NTD of hNPC1 (PDB ID: 3GKI) bound to cholesterol. **(C)** A hydrophobic, solvent-accessible pocket extends from the substrate binding pocket toward the ion coordination site. **(D)** Superposition of the NTD bound to ergosterol (PDB ID: 9F40) with the cryo-EM structures of full-length NCR1 (PDB IDs: 8QEB at pH 7.5, 8QEC and 8QED both at pH 5.5).

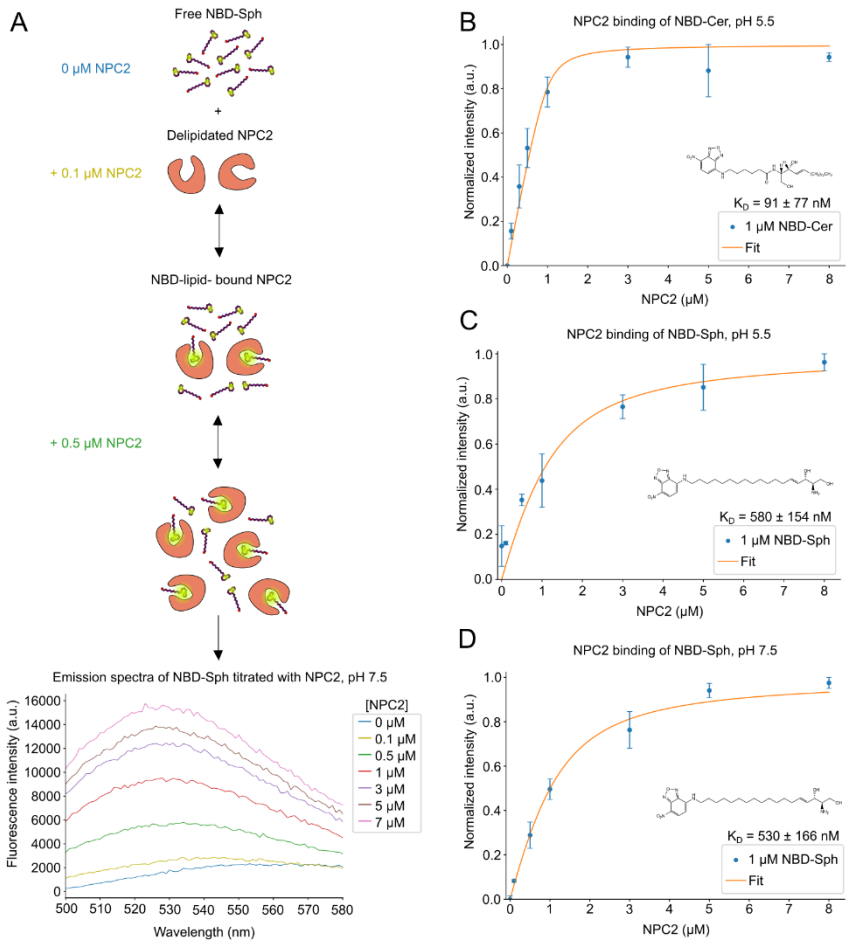

Figure S3. NBD-tagged sphingolipids bind to NPC2

(A) An overview of the principle behind the fluorescence binding assay. The graph shows representative raw emission spectra in a range of 500 nm to 580 nm of NBD-Sphingosine (NBD-Sph), measured with varying concentrations of NPC2. Measurements were conducted at an excitation wavelength of 460 nm. The dissociation constant (K_D) is 91 ± 77 nM. Data points show mean ± standard error of mean (SEM) of three (n = 3) independent experiments. **(B, C)** Normalized fluorescent signal for NBD-sphingosine show increasing fluorescence intensity because of binding to increasing concentrations of NPC2 at pH 5.5 **(B)** or pH 7.5 **(C)**. Data is shown at an excitation wavelength of 460 nm and an emission wavelength of 530 nm. The K_D-values are 580 ± 154 nM at pH 5.5 and 530 ± 166 nM at pH 7.5. Data points show mean ± SEM of three (n = 3) independent experiments.

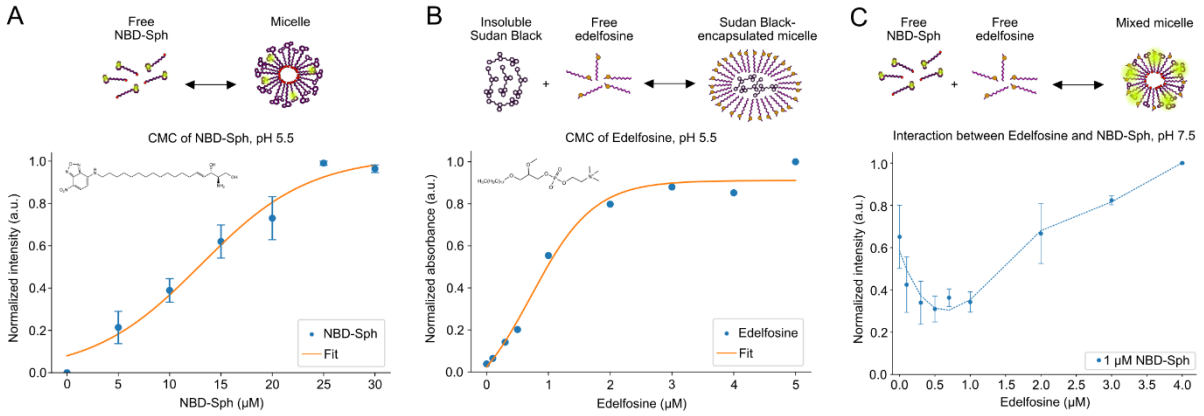

Figure S4. Critical micelle concentrations of NBD-sphingosine and edelfosine

(A) Normalized fluorescence intensity of NBD-sphingosine (NBD-Sph) at different concentrations in MES buffer at pH 5.5. Excitation and emission wavelengths were 460 nm and 530 nm, respectively. The critical micelle concentration (CMC) is determined to be 13 μM. Data points show mean ± standard error of mean (SEM) of three (n = 3) independent experiments. **(B)** Normalized absorbance of Sudan Black B at increasing concentrations of edelfosine in MES buffer at pH 5.5. The absorbance wavelength was 600 nm. The CMC of edelfosine is estimated to be 0.7 μM, however, the micelle formation might occur gradually as the concentration increases and start at the lowest concentration of 0.1 μM. The data is based on one (n = 1) experiment. **(C)** Normalized intensity of NBD-Sph when mixed with varying concentrations of edelfosine. As the concentration of edelfosine exceeds the suggested CMC, an increase in fluorescence of NBD-Sph occurs. Data is shown at excitation and emission wavelengths of 460 nm and 530 nm, respectively. Data points show mean ± SEM of two (n = 2) independent experiments.

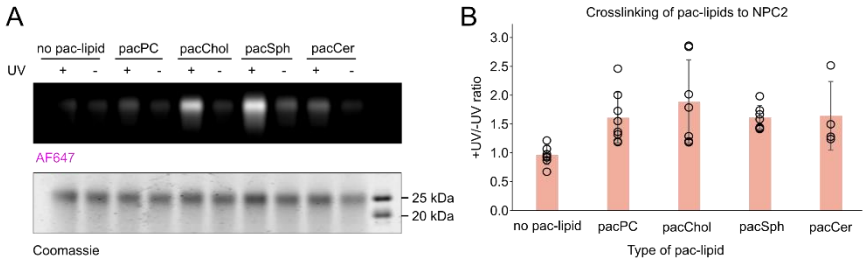

Figure S5. NPC2 crosslinking with pac-lipids

(A) Representative gel image with crosslinking profile of purified NTD. Liposomes containing 1.5 mol% of indicated pac-lipids (1 µM pac-lipid) were incubated with 1.5 µM NPC2 and UV-crosslinked. Protein-lipid complexes were subjected to click reaction with AF647-picolyl azide and visualized by SDS-PAGE. In-gel fluorescence of AF647 was normalized to loaded protein in each well based on Coomassie staining. **(B)** Normalized in-gel fluorescence is quantified as +UV/-UV signal ratio. N = at least 4 independent experiments.

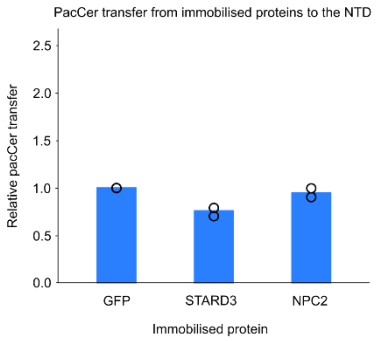

Figure S6. Quantification of normalized in-gel fluorescence of pacCer transfer assay

PacCer transfer assay was performed in the same way as pacSph transfer assay described in Figure 6. N = 2 independent experiments.

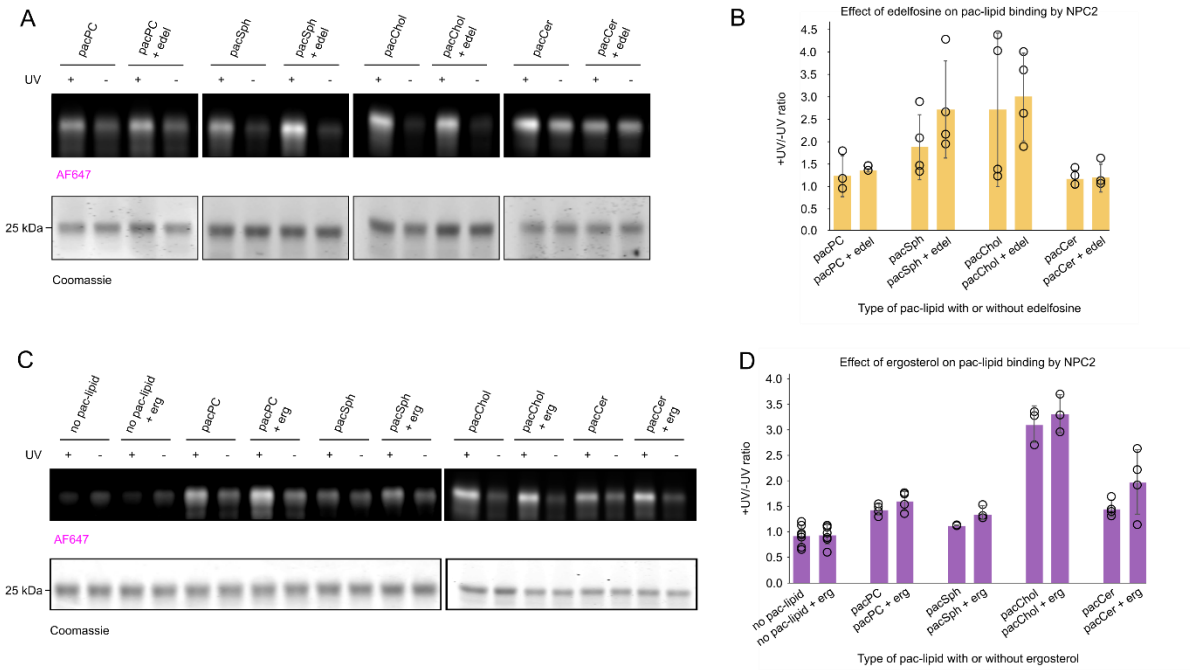

Figure S7. Impact of edelfosine and ergosterol on NPC2 crosslinking with pac-lipids
(A) Representative gel image with results of a crosslinking assay. Liposomes containing 1.5 mol% of indicated pac-lipids were supplemented with 7.5 mol% edelfosine (final concentration 1 µM pac-lipid and 5 µM edelfosine), incubated with 1.5 µM NPC2 and UV-crosslinked. Protein-lipid complexes were subjected to click reaction with AF647-picolyl azide and visualized by SDS-PAGE. In-gel fluorescence of AF647 was normalized to loaded protein in each well based on Coomassie staining. **(B)** Normalized in-gel fluorescence is quantified as +UV/-UV signal ratio. N = at least 4 independent experiments. **(C)** Representative gel image with results of a crosslinking assay. Liposomes containing 1.5 mol% of indicated pac-lipids supplemented with 20 mol% ergosterol (final concentration is thus 1 µM pac-lipid and 13 µM ergosterol). The assay was carried out as described in (A). **(D)** Quantification of normalized +UV/-UV signal, as described in (B). N = at least 4 independent experiments.

Table S1. X-ray crystallography data collection and refinement statistics.

Dataset	**NCR1-NTD bound to ergosterol**	**NCR1-NTD bound to cholesterol**
Type	Native	Native
Data collection		
Space group	P 2_1 2 2_1	P 2_1 2 2_1
Cell dimensions		
a, b, c (Å)	92.76; 109.58; 151.81	92.03; 109.78; 151.36
α, β, γ (°)	90; 90; 90	90; 90; 90
Monomers per asymmetric unit	4	4
Wavelength (Å)	0.9686	0.9763
Number of reflections measured		
Total	435345 (41561)*	391689 (36093)
Unique	58247 (5721)	45554 (4305)
Resolution range (Å)[a]	45.05-2.44 (2.527-2.44)	47.14-2.641 (2.735-2.641)
R_{meas} (%)	0.09363 (1.84)	0.1316 (2.339)
Mean I/σ (I)	12.19 (0.95)	11.39 (0.79)
CC½	99.9 (55.7)	99.9 (45.9)
Multiplicity	7.5 (7.3)	8.6 (8.4)
Completeness (%)	99.67 (99.91)	98.86 (91.66)
Wilson B-factor (Å)	69.94	76.56
Refinement		
Number of reflections (work/free)	58103/2096 (5718/205)	45255/4133 (2082/190)
R_{work} (%)	21.42 (39.17)	22.05 (37.12)
R_{free} (%)	25.72 (43.41)	25.37 (38.92)
Number of atoms		
Protein	888	888
Ligands	1033	1026
Solvent	194	193
Average B-factor		
Macromolecules	80.94	85.43
Ligands	119.20	129.64
Solvent	82.53	83.93
RMSD		
Bond lengths (Å)	0.007	0.007
Bond angles (°)	0.95	0.94
Ramachandran statistics (%)		
Favored	97.73	97.50
Allowed	2.27	2.39
Disallowed	0.00	0.11
Clashscore	2.59	3.81
Number of TLS groups	1	1
Deposited model PDB ID	9F40	9F41

Values in brackets are indicative of the highest resolution shell. Only the first instance is indicated*.
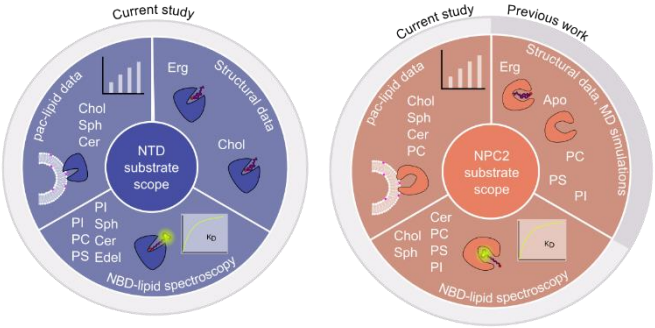
GRAPHICAL ABSTRACT